DURABLE, IMPERMEABLE BRAZES FOR SOLID OXIDE FUEL CELLS
FINAL REPORT

Report Type:	Final Report
Reporting Period Start Date:	10/1/2014
Reporting Period End Date:	9/30/2018
Principle Investigators/Authors:	Dr. Jason D. Nicholas, jdn@msu.edu, (517) 355-1615 Dr. Yue Qi, yueqi@egr.msu.edu, (517) 432-1243 Dr. Thomas R. Bieler, bieler@egr.msu.edu, (517) 366-1505
Principle Investigators/Authors Affiliation:	Chemical Engineering and Materials Science Department Michigan State University 428 South Shaw Lane Room 2527 Engineering Building East Lansing, MI 48824
Date Report was Issued:	2/11/2019
DOE Award Number:	DE-FE0023315
DUNS Number:	193247145
Name and Address of Submitting Organization:	Michigan State University 426 Auditorium Road Room 2 Administration Building East Lansing, MI 48824
Submitted by:	

1. Abstract

To develop a new braze to replace the current state-of-the-art Ag-CuO reactive air braze (RAB), two approaches were proposed: 1) development of a new, self-passivating, silver-free braze and 2) development of a CuO-free, silver-based braze.

For the first approach, an integrated computational-experimental method was used. Thermo-Calc® was utilized to quickly screen through hundreds of alloy systems to identify candidate braze compositions with the appropriate melting ranges. Material compositions, melting ranges, mechanical properties, oxidation resistance, and wetting characteristics of the candidate alloys were then analyzed experimentally. Substrate surface pre-treatments, active element additions, and novel brazing schemes were also investigated. Unfortunately, the current study failed to identify new silver-free braze compositions suitable for SOFC applications.

To help measure the passivation characteristics of surface passivating braze oxide coatings, work was conducted to demonstrate, for the first time, that a variety of disparate and technologically-relevant thermal, mechanical, and electrochemical oxygen-exchange thin film material properties could all be obtained from *in situ*, current-collector-free wafer curvature measurements. Specifically, temperature or oxygen partial pressure induced changes in the curvature of 230 nm thick (100)-oriented $Pr_{0.1}Ce_{0.9}O_{1.95\_x}$ (10PCO) films atop 200 mm thick single crystal yttria stabilized zirconia or magnesium oxide substrates were used to measure the biaxial modulus, Young's modulus, thermal expansion coefficient, thermochemical expansion coefficient, oxygen nonstoichiometry, chemical oxygen surface exchange coefficient, oxygen surface exchange resistance, thermal stress, chemical stress, thermal strain, and chemical strain of the model mixed ionic electronic conducting material 10PCO. The (100)-oriented thin film 10PCO thermal expansion coefficient, thermo-chemical expansion coefficient, oxygen nonstoichiometry, and Young's modulus (which is essentially constant, at ~200 MPa, over the entire 280–700 ºC temperature range in air) measured here were similar to those from other bulk and thin film 10PCO studies. In addition, the measured PCO10 oxygen surface coefficients were in agreement with those reported by other in situ, current collector- free techniques. However, the measured PCO10 oxygen surface exchange coefficients were significantly lower than those obtained from literature studies with large amounts of intentional or inadvertent precious metal surface coverage/contamination (suggesting that uncontaminated (100)-oriented 10PCO may not be a desirable SOFC cathode material). Taken together, this highlighted the advantages of using a sample's mechanical response, instead of the more traditional electrical response, to probe the electrochemical properties of the ion-exchange materials used in solid oxide fuel cell, solid oxide electrolysis cell, gas-sensing, battery, emission control, water splitting, water purification, and other electrochemically-active devices.

For the second approach, a novel silver-nickel brazing method was developed. It was demonstrated that transient porous nickel interlayers, instead of reactive element additions, could be used to promote Ag wetting on yttria stabilized zirconia (YSZ) and produce high-quality YSZ-stainless steel (SS) braze joints. Mechanical tests on these reactive-element-free, silver-based SOFC braze joints, both before and after 500 hours of 750°C oxidation in air, showed that the braze and braze interface strength were higher than the underlying YSZ|NiO-YSZ substrate. The microstructural and compositional evolution of SS|Ag-Ni|YSZ braze joints exposed to dual atmosphere (air on one side and 4%H_2-96%N_2 on the other side) for 300 hours of isothermal 750 °C aging and 300 25°C/min 35-830 °C rapid thermal cycles were compared to a Ag-3CuO

braze joint. In contrast to conventional Ag-CuO RAB brazes, the Ag-Ni brazes remained pore free and well bonded, suggesting that Ag-Ni brazes may be more suitable for long term SOFC operation than Ag-CuO brazes. Other applications inspired by the silver-nickel wetting process on various ceramic substrates were also explored.

In support of efforts to identify new CuO-free Ag-based brazes, density functional theory and ab initio molecular dynamics calculations were performed to 1) understand silver wetting on YSZ, and 2) identify new oxides to promote silver wetting on YSZ. These simulations found that while the formation of dissolved oxygen clusters within molten silver at the YSZ interface promoted wetting, much greater wetting angle reductions came from the formation of metal oxide interlayers at the Ag-YSZ interface. Through the development of a simple descriptor, many simple metal oxides (single cation) were examined. Unfortunately, their ability to promote Ag wetting were less than that of CuO. However, expanding the search to multi-cation oxides led to several promising candidates, such as $CuAlO_2$, $CuGaO_2$, and Cu_3TiO_4; all of which are also stable in the reducing SOFC conditions. Depending upon their solubility in molten Ag, these newly-identified oxides could either be pre-applied as wetting promoting interlayers or directly incorporated into Ag to form new reactive air brazes.

2. Table of Contents

3. Executive Summary

Two approaches were proposed to develop a replacement braze for the current state-of-the-art RAB (Ag-CuO) braze. One was a high risk approach to design a new, silver-free braze that self passivates during SOFC operation (much like stainless steel that forms a passivating chromia layer that prevents oxidation of the underlying metal). The other was a lower risk approach to develop a CuO-free, silver-based braze that eliminates some of the degradation mechanisms active in the common Ag-CuO brazes.

For the first approach, an integrated computational-experimental method was used. Candidate braze alloys with excellent oxidation resistance and suitable melting ranges were identified. Also, it was demonstrated, for the first time, that wafer curvature measurements could be used to obtain a variety of oxygen passivation or oxygen transport material properties. Unfortunately, due to time constraints, the current study failed to find a suitable silver-free braze with the needed wetting characteristics.

For the second approach, a novel silver-nickel brazing method was invented. In addition, simulations identifying several new, alternative oxides to promote silver wetting on yttria stabilized zirconia were identified. It was demonstrated that transient porous nickel interlayers, instead of reactive element additions, could be used to promote Ag wetting on YSZ and produce high-quality YSZ-stainless steel braze joints. The mechanical strength of these Ag-Ni braze joints were shown to be sufficient for Delphi's SOFCs. Additional dual atmosphere studies also showed the much better operational reliability of the newly developed Ag-Ni braze compared to conventional Ag-CuO brazes.

Three papers were published, and four more are in preparation, to disseminate the scientific progress achieved in this project. These paper topics included 1) wafer curvature studies to measure the thermo-mechanical, chemical properties of SOFC materials, 2) computational studies on the wetting and interfacial properties of silver-based brazes with interfacial oxide additions, 3) Ag-Ni braze joint fabrication and dual atmosphere longevity, and 4) the fabrication of Ag-Ni circuits. Two US patent applications were also filed based on the work pursued in this project.

4. Accomplishments

Major Project Goals

The overall goal of the proposed work was to use a combined simulation-experimental approach to design and test new, silver-free brazes that form durable, oxygen impermeable protective surface scales. To achieve this overall result, the following objectives were pursued:

Objective 1: Identify New Brazes with Manufacturing-Compatible Liquidus Temperatures
Objective 2: Identify those Brazes Forming Chemically-stable, CTE-compatible Surface Oxides
Objective 3: Produce Brazes with Appropriate Wetting Angles
Objective 4: Produce Brazes with Strong Metallurgical Bonding to the Surrounding Material, High Braze Joint Strength, and Sufficient Ductility
Objective 5: Produce Brazes with Low-Vapor Pressure Protective Scales that Impart High Temperature Oxidation Resistance to the Braze and Block Hydrogen Transport
Objective 6: Produce Brazes Suitable for 40,000 Hours of SOFC Operation at 750°C

Milestone Status Report

Milestone	Description	Planned Completion Date	Actual Completion Date	Verification Method	Key Accomplishments
1	Calculate promising nickel alloy-oxygen phase diagrams	3/1/2015	3/1/2015	Experiments on select compositions	By systemically considering evaporation temperature, radioactivity, reactivity, toxicity, and cost, 37 elements (Mg, Al, Si, Ti, V, Cr, Mn, Fe, Co, Ni, Cu, Zn, Ga, Ge, Y, Zr, Nb, Mo, Ag, In, Sn, Sb, I, La, Ce, Pr, Nd, Sm, Gd, Dy, Ho, Er, Yb, Hf, Ta, W, Bi) were identified as possible alloy components. This analysis identified some surprising Ni-based alloys that melt between 900 and 1000°C. However since all these alloys exhibited poor wetting, work on these non-silver based brazes was halted.
2	Calculate other eutectic phase diagrams	3/1/2015	3/1/2016	Experiments on select compositions	
3	Measure the physical properties, microstructures, and interface strengths of promising alloys identified in Milestones 1 & 2	6/1/2016	9/30/2018	Cross-check DSC and brazing furnace temperatures, Correlating measured interface strengths with rapid thermal cycling results	To circumvent Ag-based braze wetting problems, we perfected a new porous nickel interlayer brazing approach and used a newly developed wetting angle and bond strength computation framework to search for oxides promoting braze wetting. We demonstrated that the Ni-Ag produced high quality braze joints that performed better than conventional Ag0CuO joints in dual atmosphere isothermal and/or rapid thermal cycling tests.
4	Send promising, high-risk samples to Delphi for manufacturing compatibility testing	6/1/2016	7/1/2018	Correlate Delphi experiences with laboratory results	The Ni-Ag brazes were evaluated at Delphi (now Aptiv). In Q16, Delphi officially liquidated and closed its Fenton, MI facility, formally ending its SOFC Program.

5	Measure surface scale passivation ability	3/1/2017	9/30/2018	Correlate O_2 surface exchange and TGA measurements	Since we switched to silver-based brazes that don't form a passivating surface oxide in air (but now benefit from porous nickel interlayers) there was no need to measure the surface scale passivation ability. However, our work on oxygen surface exchange funded with this award allowed us to demonstrate for the first time that *in situ* wafer curvature measurements could be used to easily obtain a MIEC's oxygen surface exchange coefficient, Young's Modulus, thermo-chemical expansion coefficient, oxygen nonstoichiometry, and oxygen surface exchange resistance in situ.
6	Send promising, low-risk samples to Delphi for manufacturing compatibility testing	3/1/2017	7/1/2018	Correlate Delphi experiences with laboratory results	The Ni-Ag brazes were evaluated at Delphi (now Aptiv). In Q16, Delphi officially liquidated and closed its Fenton, MI facility, formally ending its SOFC Program.
7	Identify the specific braze compositions and processing conditions necessary to produce a reliable SOFC braze	9/1/2017	9/30/2018	Correlate Delphi experiences with laboratory results	The Ni-Ag brazes were evaluated at Delphi (now Aptiv) and were shown to be more durable than conventional Ag-CuO brazes. In Q16, Delphi officially liquidated and closed its Fenton, MI facility, formally ending its SOFC Program.

5. Report Details

5.1 Integrated Computational Materials Design for Silver-free Brazes

5.1.1 Candidate Braze Alloy Selection

Here, ThermoCalc modeling was used to computationally identify binary alloys with liquidus and solidus temperatures compatible with Delphi's SOFC manufacturing processes (i.e. brazes with liquidus temperatures at or below 1000ºC and solidus temperatures at or above ~900ºC), with the thinking that minor alloy additions could be used to alter the wetting, oxidation resistance, and interface strength properties, as needed, to produce high-quality braze joints. The final Thermocalc search space included not only ternary nickel based alloy systems, but also ternary cobalt and ternary copper based alloys systems. These results, summarized in Tables 1-3, indicated that a variety of nickel, copper, or cobalt based alloys with the desired melting ranges exist. In these tables, red fill indicates ternary alloys systems disqualified for lacking liquidus regions at or below 1000˚C, blue fill indicates ternary alloy systems disqualified for lacking solidus regions at or below 900˚C, green fill indicates promising ternary alloy systems with at least one composition that was liquid or liquid + solid at or below 1000˚C and solid below 900˚C, and white fill indicates a lack of Thermocalc information for that system. Table 1 shows that 19 nickel-based ternary alloy systems (Ni-B-(Y), Ni-(Cr,W)-Ti, Ni-Fe-(Ti, Zr), Ni-Si-(Cr, Sn, Ta, Hf), Ni-Mn-(Si, Nb, Mo, Ta, Zr, Hf, C, B), and Ni-Zr-(Al,V)) met the desired liquidus and solidus temperature requirements. Similarly, Table 2 shows that 31 cobalt-based ternary alloy systems (Co-V-(B, Si), Co-Fe-B, Co-Ni-(B, Si), Co-Nb-B, Co-Mo-Si, Co-Ni-Sn, Co-Ta-(B, Mn), Co-Ti-(Si, Cr, Mn, Fe, Ni, Nb), Co-Ti-Y, Co-Zr-(B, C, Si, V, Cr, Fe, Ni, Nb, Mo, W), Co-Zr-Hf, and Co-Ag-(Al, Cu, In)) met the desired liquidus and solidus temperature requirements. Lastly, Table 3 shows that, thanks to the low melting point of Cu, 64 copper-based ternary alloy systems met the desired liquidus and solidus temperature requirements.

Table 1 Nickel-Based Ternary Alloys Systems of Potential Interest for SOFC Braze Applications

Ni	B	C	Mg	Al	Si	V	Cr	Mn	Fe	Co	Cu	Zn	Ga	Nb	Mo	In	Sn	Ta	W	Ti	Y	Zr	Hf	Ag
B																								
C	Ni-B-C																							
Mg	Ni-B-Mg	Ni-C-Mg																						
AL	Ni-B-AL	Ni-C-AL	Ni-Mg-AL																					
Si	Ni-B-Si	Ni-C-Si	Ni-Mg-Si	Ni-Al-Si																				
V	Ni-B-V	Ni-C-V	Ni-Mg-V	Ni-Al-V	Ni-Si-V																			
Cr	Ni-B-Cr	Ni-C-Cr	Ni-Mg-Cr	Ni-Al-Cr	Ni-Si-Cr	Ni-V-Cr																		
Mn	Ni-B-Mn	Ni-C-Mn	Ni-Mg-Mn	Ni-Al-Mn	Ni-Si-Mn	Ni-V-Mn	Ni-Cr-Mn																	
Fe	Ni-B-Fe	Ni-C-Fe	Ni-Mg-Fe	Ni-Al-Fe	Ni-Si-Fe	Ni-V-Fe	Ni-Cr-Fe	Ni-Mn-Fe																
Co	Ni-B-Co	Ni-C-Co	Ni-Mg-Co	Ni-Al-Co	Ni-Si-Co	Ni-V-Co	Ni-Cr-Co	Ni-Mn-Co	Ni-Fe-Co															
Cu	Ni-B-Cu	Ni-C-Cu	Ni-Mg-Cu	Ni-Al-Cu	Ni-Si-Cu	Ni-V-Cu	Ni-Cr-Cu	Ni-Mn-Cu	Ni-Fe-Cu	Ni-Co-Cu														
Zn	Ni-B-Zn	Ni-C-Zn	Ni-Mg-Zn	Ni-Al-Zn	Ni-Si-Zn	Ni-V-Zn	Ni-Cr-Zn	Ni-Mn-Zn	Ni-Fe-Zn	Ni-Co-Zn	Ni-Cu-Zn													
Ga	Ni-B-Ga	Ni-C-Ga	Ni-Mg-Ga	Ni-Al-Ga	Ni-Si-Ga	Ni-V-Ga	Ni-Cr-Ga	Ni-Mn-Ga	Ni-Fe-Ga	Ni-Co-Ga	Ni-Cu-Ga	Ni-Zn-Ga												
Nb	Ni-B-Nb	Ni-C-Nb	Ni-Mg-Nb	Ni-Al-Nb	Ni-Si-Nb	Ni-V-Nb	Ni-Cr-Nb	Ni-Mn-Nb	Ni-Fe-Nb	Ni-Co-Nb	Ni-Cu-Nb	Ni-Zn-Nb	Ni-Ga-Nb											
Mo	Ni-B-Mo	Ni-C-Mo	Ni-Mg-Mo	Ni-Al-Mo	Ni-Si-Mo	Ni-V-Mo	Ni-Cr-Mo	Ni-Mn-Mo	Ni-Fe-Mo	Ni-Co-Mo	Ni-Cu-Mo	Ni-Zn-Mo	Ni-Ga-Mo	Ni-Nb-Mo										
In	Ni-B-In	Ni-C-In	Ni-Mg-In	Ni-Al-In	Ni-Si-In	Ni-V-In	Ni-Cr-In	Ni-Mn-In	Ni-Fe-In	Ni-Co-In	Ni-Cu-In	Ni-Zn-In	Ni-Ga-In	Ni-Nb-In	Ni-Mo-In									
Sn	Ni-B-Sn	Ni-C-Sn	Ni-Mg-Sn	Ni-Al-Sn	Ni-Si-Sn	Ni-V-Sn	Ni-Cr-Sn	Ni-Mn-Sn	Ni-Fe-Sn	Ni-Co-Sn	Ni-Cu-Sn	Ni-Zn-Sn	Ni-Ga-Sn	Ni-Nb-Sn	Ni-Mo-Sn	Ni-In-Sn								
Ta	Ni-B-Ta	Ni-C-Ta	Ni-Mg-Ta	Ni-Al-Ta	Ni-Si-Ta	Ni-V-Ta	Ni-Cr-Ta	Ni-Mn-Ta	Ni-Fe-Ta	Ni-Co-Ta	Ni-Cu-Ta	Ni-Zn-Ta	Ni-Ga-Ta	Ni-Nb-Ta	Ni-Mo-Ta	Ni-In-Ta	Ni-Sn-Ta							
W	Ni-B-W	Ni-C-W	Ni-Mg-W	Ni-Al-W	Ni-Si-W	Ni-V-W	Ni-Cr-W	Ni-Mn-W	Ni-Fe-W	Ni-Co-W	Ni-Cu-W	Ni-Zn-W	Ni-Ga-W	Ni-Nb-W	Ni-Mo-W	Ni-In-W	Ni-Sn-W	Ni-Ta-W						
Ti	Ni-B-Ti	Ni-C-Ti	Ni-Mg-Ti	Ni-Al-Ti	Ni-Si-Ti	Ni-V-Ti	Ni-Cr-Ti	Ni-Mn-Ti	Ni-Fe-Ti	Ni-Co-Ti	Ni-Cu-Ti	Ni-Zn-Ti	Ni-Ga-Ti	Ni-Nb-Ti	Ni-Mo-Ti	Ni-In-Ti	Ni-Sn-Ti	Ni-Ta-Ti	Ni-W-Ti					
Y	Ni-B-Y	Ni-C-Y	Ni-Mg-Y	Ni-Al-Y	Ni-Si-Y	Ni-V-Y	Ni-Cr-Y	Ni-Mn-Y	Ni-Fe-Y	Ni-Co-Y	Ni-Cu-Y	Ni-Zn-Y	Ni-Ga-Y	Ni-Nb-Y	Ni-Mo-Y	Ni-In-Y	Ni-Sn-Y	Ni-Ta-Y	Ni-W-Y	Ni-Ti-Y				
Zr	Ni-B-Zr	Ni-C-Zr	Ni-Mg-Zr	Ni-Al-Zr	Ni-Si-Zr	Ni-V-Zr	Ni-Cr-Zr	Ni-Mn-Zr	Ni-Fe-Zr	Ni-Co-Zr	Ni-Cu-Zr	Ni-Zn-Zr	Ni-Ga-Zr	Ni-Nb-Zr	Ni-Mo-Zr	Ni-In-Zr	Ni-Sn-Zr	Ni-Ta-Zr	Ni-W-Zr	Ni-Ti-Zr	Ni-Y-Zr			
Hf	Ni-B-Hf	Ni-C-Hf	Ni-Mg-Hf	Ni-Al-Hf	Ni-Si-Hf	Ni-V-Hf	Ni-Cr-Hf	Ni-Mn-Hf	Ni-Fe-Hf	Ni-Co-Hf	Ni-Cu-Hf	Ni-Zn-Hf	Ni-Ga-Hf	Ni-Nb-Hf	Ni-Mo-Hf	Ni-In-Hf	Ni-Sn-Hf	Ni-Ta-Hf	Ni-W-Hf	Ni-Ti-Hf	Ni-Y-Hf	Ni-Zr-Hf		
Ag	Ni-B-Ag	Ni-C-Ag	Ni-Mg-Ag	Ni-Al-Ag	Ni-Si-Ag	Ni-V-Ag	Ni-Cr-Ag	Ni-Mn-Ag	Ni-Fe-Ag	Ni-Co-Ag	Ni-Cu-Ag	Ni-Zn-Ag	Ni-Ga-Ag	Ni-Nb-Ag	Ni-Mo-Ag	Ni-In-Ag	Ni-Sn-Ag	Ni-Ta-Ag	Ni-W-Ag	Ni-Ti-Ag	Ni-Y-Ag	Ni-Zr-Ag	Ni-Hf-Ag	

No liquid phase present in the phase diagram below 1000 °C

There exists some specific composition zone, which completely solidifies from liquid phase, between temperature window of 900 and 1000 °C

The composition of liquid zone at 1000 °C, remains liquid or solid+liquid below 900 °C

Not available in database

Table 2. Cobalt-Based Ternary Alloys Systems f Potential Interest for SOFC Braze Applications

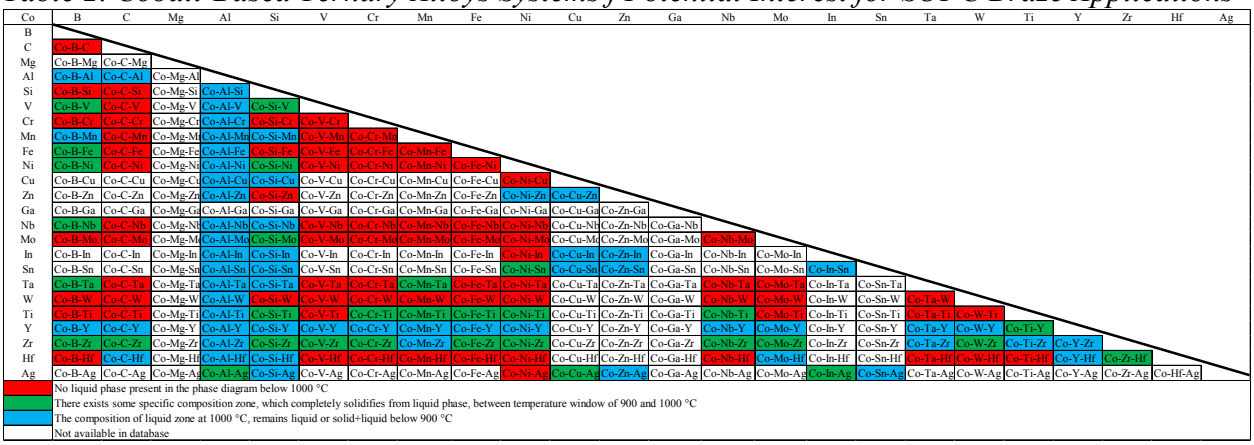

Table 3. Copper-Based Ternary Alloys Systems of Potential Interest for SOFC Braze Applications

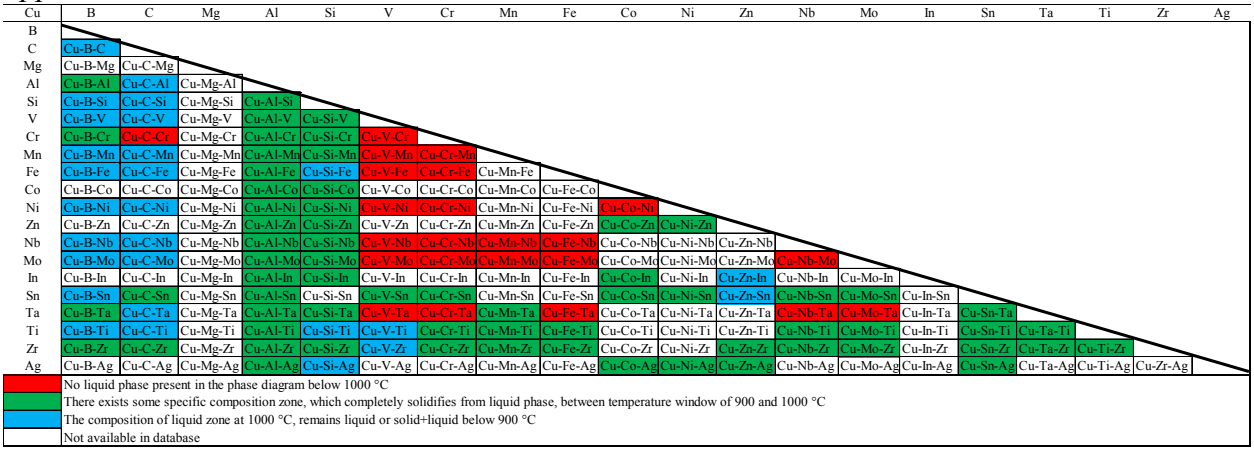

5.1.2 Select Physical Properties of Experimentally Characterized Alloys

As shown in Table 4, 43 alloys from the green alloy systems shown in Tables 1-3 were experimentally produced and tested. Of these, a variety of Ni-Si and Cu-Al based alloys displayed suitable ductility, oxidation resistance, and melting point characteristics. The suitability of these particular alloy systems came as little surprise since Ni-Si and Cu-Al serve as the basis, respectively, of the BNi and Cu-ABA families of commercially available brazes. However, prior to the work in this award it was unknown that Ta, with a melting point of 3020ºC, could be used as a Ni-Si alloy melting point depressant (lowering the 1214ºC liquidus temperature of Ni10Si by ~60ºC).

Table 4. Ductility, Oxidation Resistance, and Melting Temperatures for a Variety of Nickel-Based, Cobalt-Based, and Copper-Based Alloys.

Alloy Composition	Ductility	48 hr 750°C Oxidation Resistance in Air	Solidus Temperature @ 5k/min	Liquidus Temperature	Comments
Ni43.5Mn14.8Nb	Sufficient	Poor			
Ni48.5Mn14.6Mo	Sufficient	Poor			
Ni50Mn5Si	Insufficient	Poor			
Ni36.9Mn11Si	Insufficient				
Ni52.2Mn10.9Ta	Sufficient	Poor			
Ni26.0Mn22.4Si	Insufficient				
Ni4.5Si7.0Cr3.1B 3.0Fe (Commercial BNi2 Containing Iron)	Sufficient	Excellent	Excellent (970.0)	Excellent (1000.0)	Promising Braze if Cr Volatilization Can be Managed
Ni5Si2Cr60Al	Insufficient				
Ni5Si20Ta	Sufficient	Poor	Too High (1132.0)	Too High (1138.0)	
Ni7Si20Ta	Sufficient	Good	Too High (1124.8)	Too High (1139.1)	
Ni7Si20Ta1B	Sufficient	Good	Good (1035.9)	Good (1068.0)	Solidus/Liquidus may be workable.
Ni7Si20Ta3B	Insufficient	Good	Good (1051.0)	Good (1086.8)	Needs improvement in ductility
Ni10Si20Ta	Insufficient	Excellent	Too High (1144.0)	Too High (1162.9)	
Ni7Si32Ta1B	Sufficient	Good	Good (1041.2)	Good (1070.1)	Wetting on alumina and zirconia is inherently poor
Ni7Si32Ta	Sufficient	Marginal	Too High (1122.7)	Too High (1146.1)	
Ni7Si25Ta	Sufficient		Too High (1127.4)	Too High (1137.9)	
Ni7Si10Ta	Sufficient		Too High (1124.6)	Too High (1140.3)	Solid solution
Ni71.5Ti	Sufficient	Extremely Poor			
Ni41Ti17Nb2Al	Marginal	Fair			
Ni41Ti17Nb3Al	Marginal	Poor			
Ni41Ti17Nb5Al	Sufficient	Fair			
Ni42.5Zr2Al3.5Si	Sufficient	Poor			
Ni9Zr11Nb4Si	Sufficient	Poor			
Ni35Zr13.3Y	Sufficient	Extremely Poor			
Ti15Ni15Fe	Marginal	Poor	Good (1020.4)	Good (1037.7)	Excellent Wetting on Pure Al_2O_3
Ti32Ni8Cr	Marginal	Poor	Good (1013.3)	Good (1025.1)	Excellent Wetting on Pure Al_2O_3
Ni17Zr5.5Al	Marginal	Poor	Too High (1187.4)	Too High (1221.4.4)	

Ni15Zr3.5Si2Al	Marginal	Poor	Good (1060.4)	Good (1066.2)	Sample reacted with crucible during DSC measurement
Ni30In5Zn	Sufficient	Good	Good (917.1)	Good (923.1)	Zn/In will vaporize at high temperature
Ni41.4In (eutectic)	Insufficient	Good	Good (916.0)	Good (926.2)	In vaporize at high temperature. Does not wet pure Al_2O_3
Al15Ni15Ti6Si4Cr	Poor				
Ti41Ni18Nb	Sufficient	Poor			
Ag10Cr					Ag and Cr are hard to mix during arc melting
Ag20Cr					
Ni10Ta7Si1B	Sufficient	Excellent	Good (1037.6)	Good (1074.3)	
Ni10Si	Sufficient	Excellent	Too High (1214.7)	Too High (1222.5)	
Ni10Si1B	Sufficient	Excellent	Good (1001.4)	Good (1032.8)	
Ni7Ta2Si	Sufficient	Poor			
Ni20Cu10Si		Excellent			
Cu1.5Cr	Excellent		Good (1073.3)	Good (1085.9)	
Cu5Si	Excellent		Good (956.3)	Good (974.0)	
Cu9Al	Excellent	Good	Good (1034.1)	Good (1047.5)	
Ni6Co5Si	Excellent	Good	Too High (>1300)	Too High (>1300)	

5.1.3 Oxidation Resistance of Top Candidate Alloys

As shown in Figure 1, to further study the oxidation behavior of some of the most promising braze alloys (which by definition exhibit low, hard-to-measure oxidation rates) 5-day oxidation tests (in addition to the 2-day oxidation tests summarized in Table 4) were conducted. These results showed that a variety of Ni-Si based brazes (Ni20Cu10Si, Ni20Ta7Si1B, Ni10Si1B, etc.) possessed oxidation resistances similar to commercially available BNi2, but did not contain the Cr known to poison LSM, LSCF and other SOFC cathode materials [1].

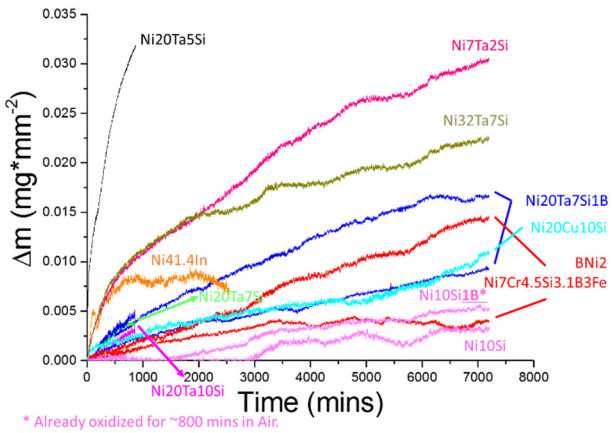

Figure 1. *Sample Surface Area Normalized Thermal-Gravimetric Analysis (TGA) Data for Different Samples Tested at 750°C in Flowing Air.*

5.1.4 In Situ Braze Wetting Studies

As shown in Figure 2, a controlled atmosphere wetting furnace was constructed to measure the wetting properties of different candidate alloys on YSZ and stainless steel. Unfortunately, none of the tested silver-free alloys wetted or bonded to Al_2O_3, stainless steel (SS) or bare yttria stabilized zirconia (YSZ) in carbon-gettered Argon.

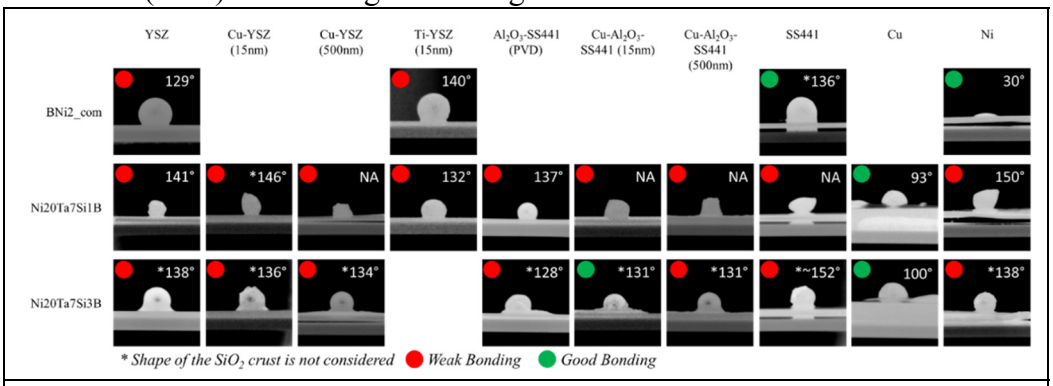

Figure 2. *Alloy Wetting on Various Bare and Metal-Sputtered Substrates at ~1080°C in Air. Alloys that could not be Pried off the Substrate after Brazing are Indicated by Green Dot.*

To improve the wetting properties, other metallization schemes, fluxing agents, brazing atmospheres, and brazing temperatures were explored. Figure 3 shows another set of wetting experiments conducted with nickel-based alloys and flux on the Al_2O_3-SS441 substrate and pure copper with and without flux additions on the YSZ|NiO-YSZ substrates. Compared to the results in Figure 2, it can be concluded that the addition of flux can significantly improve the wetting behavior of Ni20Ta7Si3B and Ni10Si1B on the alumina coated SS441 substrates. The flux composition was confidential; however, it ws very likely that the boron containing flux lowered the local partial pressure of oxygen and/or dissolved some of the surface oxides on the alloy (such as SiO_2) during the wetting and spreading process. Unfortunately, the flux was shown to embrittle the YSZ|NiO-YSZ substrate, so that its application at the YSZ interface was unacceptable. Also, as shown in Figure 3, pure copper was found to have relatively good wetting characteristics on the YSZ|NiO-YSZ substrates. The wetting sample also survived cross-sectioning

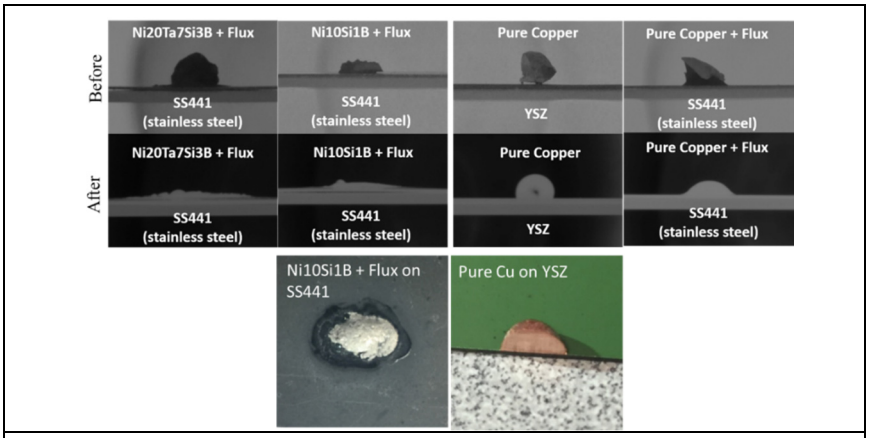

Figure 3. *Before and after images of different wetting experiments done with flux on the Al_2O_3-SS441 substrates, as well as wetting of pure copper on the YSZ|NiO-YSZ substrate with and without flux. The bottom two optical images show the surface after the Ni10Si1B+Flux wetting on the Al_2O_3-SS441 and the cross-sectioned copper on YSZ|NiO-YSZ wetting samples, respectively.*

and showed a dense, pore-free interface with YSZ. These improvements on the Al_2O_3-SS441 and YSZ|NiO-YSZ substrate lead to the design of a multi-layer brazing process, which was devised to separate the wetting problems on the two substrates into two separate parts.

5.1.5 Transient Multilayer Braze Joint Architecture

A transient multilayer braze approach allowing the brazing of alumina coated 441 to YSZ|NiO-YSZ was investigated. As shown in Figure 4a, this multilayer structure consisted of alumina-coated 441 stainless steel, braze, with a foil that remained solid during the brazing process (Ni), a YSZ wetting/bonding layer that was molten at fabrication temperatures (Cu), and YSZ|NiO-YSZ. This multiplayer brazing geometry effectively separated the brazing problem into two separate parts: (1) bonding the copper foil to the YSZ|NiO-YSZ, and (2) bonding the nickel foil to the Al_2O_3-SS441). This allowed different chemistries to be used to bond to the two substrates. Furthermore, this architecture allowed YSZ brazing to occur in one atmosphere and Al_2O_3-SS441 brazing to occur in another atmosphere. For instance, brazing of the Ni foil to the alumina coated stainless steel could be conducted under low local pO_2 environments (since the YSZ-supported SOFC cathode materials were not involved) and then the Al_2O_3-SS441|braze|Ni-foil could be bonded to YSZ in an inert atmosphere. Alternatively, as shown in Figure 3, the application of a commercial flux (HANDY FLUX HI-TEMP® Boron modified, Lucas-Milhaupt, Inc.) could also be used to braze Ni foil (and by extension most nickel-based super alloys) to the Al_2O_3-SS441substrate in Argon, without danger of flux-damage to the YSZ.

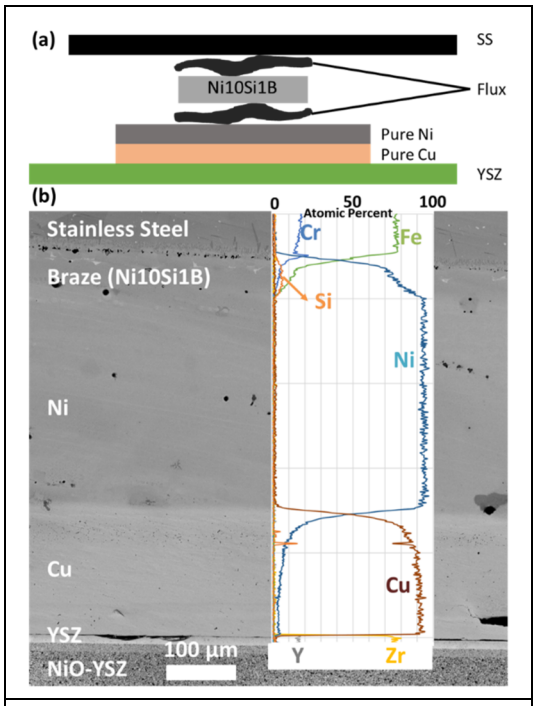

Figure 4. *(a) Schematic of the Transient Multilayer Brazing Architecture, and (b) a Backscatter Electron Image and EDS Line Scan of a Multilayer Braze Joint Cross-Section after brazing in Argon.*

Figure 4b shows a backscattered electron (BSE) image of a cross-section from the multilayer brazed joint. The different layers of materials can be observed from the EDS line scan results, and the braze region contains a Ni10Si-rich layer, a nickel-rich layer, and a copper-rich layer from the SS441 side to the YSZ side with interdiffusion occurred in-between.

Molten copper was used as the YSZ bonding agent and produced strong, reliable braze joints due to its suitable melting range and ability to wet/react with YSZ (as shown in Figure 3 and 4 as indicated in the literature [2, 3]). However, once heated in air, the volume changes associated with copper oxidation caused failure at the copper-YSZ interface. Hence, an approach to use a transient YSZ wetting layer (copper foil) was explored so that after reacting and bonding with the YSZ, the copper would inter-diffuse with the nickel layer and produces a Ni-Si-Cu alloy with a high oxidation resistance. In theory, any metal which (i) remains a molten metal (i.e. does not oxidize) at the braze temperatures and pO_2 combinations that will not harm the cathode materials and (ii) bonds with YSZ (such as Ag, Bi, etc.), could be used as a YSZ bond layer.

As shown in Figure 5, extended braze times produced partially homogenized Ni-Cu braze joints using thin copper foils with 25 µm thickness. However, due to the different diffusivities of Ni and Cu, Kirkendall voids developed which detached the braze joint from the YSZ [4]. After this result, work on silver-free SOFC braze joints was halted.

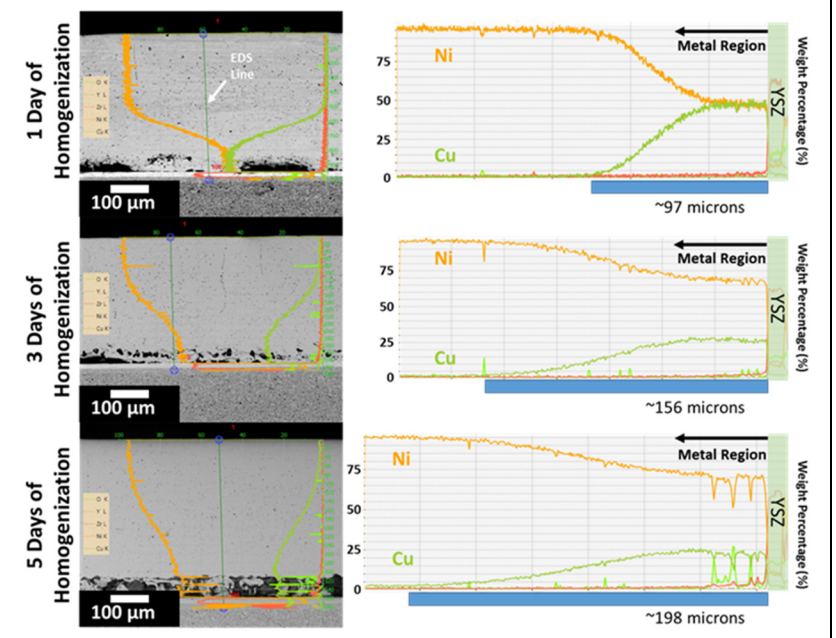

Figure 5. *(left) BSE images and (right) EDS line scan results of the 1/3/5 day homogenized Ni-Cu-YSZ|NiO-YSZ.*

5.1.6 Summary

Binary and ternary alloys with solidus temperatures equal to or greater than ~900 °C and liquidus temperatures equal to or less than ~1000 °C were identified through Thermo-Calc phase diagram calculations. All 828 of the ternary Ni-based, Co-based, and Cu-based alloy systems containing B, C, Mg, Al, Si, Ti, V, Cr, Mn, Fe, Co, Ni, Cu, Zn, Ga, Y, Zr, Nb, Mo, Ag, In, Sn, Hf, Ta, and/or W were analyzed by Thermo-Calc and 114 ternary alloy systems with the desired melting point characteristics were identified. These selected candidate compositions were then physically fabricated and various material properties were characterized. Melting point measurements with DSC, oxidation resistance evaluation with TGA and mechanical property tests on alloys in 43 of these systems found Ni-Si, Cu-Cr, and Cu-Al alloys worthy of additional study. However, further in-situ wetting studies indicated that these alloys exhibited poor wetting on both bare and also surface pre-treated YSZ|NiO-YSZ and Al_2O_3-SS441 substrates in inert gas atmospheres.

In response to these wetting challenges, a novel multilayer braze architecture was developed and the production of a high strength Al_2O_3-SS441/braze/Ni-foil/Cu-foil/YSZ|NiO-YSZ braze joint was produced in inert atmosphere. Unfortunately, this braze joint did not survive service in air due to oxidation of the copper layer. Continued efforts were spent on (1) alterative multilayer braze joint layer compositions, and (2) through the use of YSZ bonding layers that bond with the YSZ and then become protected from subsequent oxidation in air by homogenizing with other braze layers. Copper fits both of these requirements in that it can bond to the YSZ surface and also can be homogenized into the nickel layer through inter-diffusion. However, due to the different diffusivity of copper and nickel, extensive Kirkendall voids formation was observed after prolonged homogenization, which led to easy detachment at the YSZ interface.

For future investigation, it is crucial to delay the formation of the braze surface passivation layer so that it doesn't form during brazing but instead forms during normal SOFC operations. However, due to the interest of time, we moved on with a lower risk approach to improve upon the current state-of-the-art RAB braze for a CuO-free solution.

5.2 Mechanical, Thermal, and Electrochemical Properties of Pr Doped Ceria from Wafer Curvature Measurements

As mentioned previously, to help measure the passivation characteristics of surface passivating braze oxide coatings, work was conducted to demonstrate, for the first time, that a variety of disparate and technologically-relevant thermal, mechanical, and electrochemical oxygen-exchange thin film material properties could all be obtained from *in situ*, current-collector-free wafer curvature measurements. Specifically, by using *in situ* wafer curvature measurements to determine the stress (σ) vs. temperature (T) behavior of identical thin films on two substrates with very different thermal expansion coefficients (α_1 and α_2), the biaxial modulus of the film (M_f) and the thermochemical expansion coefficient of the film (α_{tc}) were determined using the definition of thermo-chemical film-substrate mismatch:

$$\frac{\partial \sigma_1}{\partial T} = M_f(\alpha_1 - \alpha_{tc}) \quad (1)$$

and

$$\frac{\partial \sigma_2}{\partial T} = M_f(\alpha_2 - \alpha_{tc}) \quad (2)$$

(where there are two equations and two unknowns; M_f and α_{tc}). Further, with knowledge of the film's Poisson ratio (v_f, which is usually close to 0.3 for most materials) the film's Young Modulus (E_f) were extracted from the film's biaxial modulus (M_f), using the biaxial modulus definition:

$$M_f = \frac{E_f}{(1-v_f)} \quad (3)$$

Once the biaxial modulus was known, the measured film stress was converted to a film strain via Hooke's Law. Then, once the thermal expansion strain was separated from the chemically induced strain (ε_C) by projecting the thermal expansion strain which is the sole cause of expansion at low temperatures to higher temperature, the film's oxygen stoichiometry (δ) was determined (assuming that oxygen stoichiometry changes were the dominant mechanism causing chemical strain) with knowledge of the film's chemical expansion coefficient (α_C) using the relationship:

$$\varepsilon_C = \alpha_C \Delta\delta \quad (4)$$

Independently, the film's chemical oxygen surface exchange coefficient (k) was determined by fitting its measured curvature relaxation (κR) to a sudden, small oxygen partial pressure change to a solution to Fick's Second Law. Using additional mathematical relationships, the film's electrical resistance for exchanging oxygen across its surface (R_S, which is often the most resistive part of SOFC operation) was also determined.

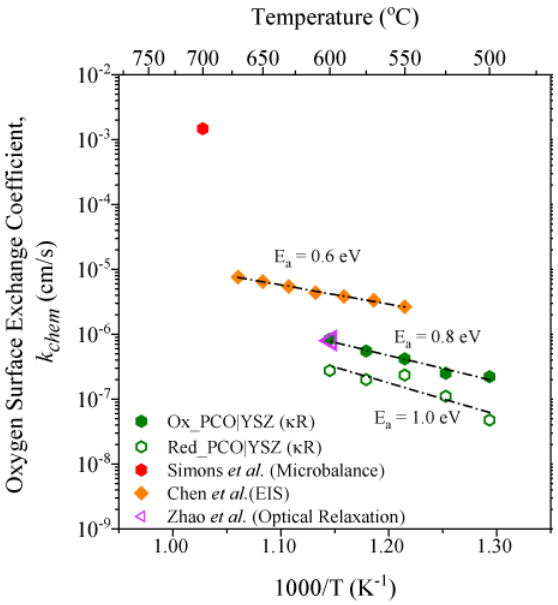

Figure 6. *10PCO chemical oxygen surface exchange coefficients from the curvature relaxation method compared to the literature measurements of Zhao et al [48], Chen et al [49], and Simons et al [50]. The curvature-determined k error is less than the size of the symbol.*

The (100)-oriented thin film $Pr_{0.1}Ce_{0.9}O_{1.95-x}$ (10PCO) thermal expansion coefficient, thermo-chemical expansion coefficient, oxygen nonstoichiometry and Young's Modulus measured using this approach were similar to those from other bulk and thin film 10PCO studies. In addition, as shown in Figure 6, the measured PCO10 oxygen surface coefficients were in agreement with those reported by other *in situ*, current-collector-free techniques (i.e. optical relaxaton studies [5]). However, the measured PCO10 oxygen surface exchange coefficients were significantly lower than those obtained from literature studies with large amounts of intentional [6] or inadvertent [7] precious metal surface coverage/contamination. This suggests that 1) a significant portion of the *k* variation observed in the literature may be caused by varying degrees of precious metal enhancement of oxygen surface exchange, and 2) that uncontaminated (100)-oriented 10PCO may not be a desirable SOFC cathode material. Since most materials experience lattice parameter changes with changes in composition, it is our hope that the techniques developed here find use for the "simultaneous" determination of the mechanical properties, thermal properties, point defect concentrations and ion-exchange properties of a variety of other ionic conducting materials.

5.3 Computational Design of Oxide Enabled Brazing on Ceramics

5.3.1 The Mechanism of Wettability Enhancement by Diffused O_2

To understand the wetting of Ag, the mechanism by which dissolved O_2 enhances the wettability of Ag(*l*) on YSZ was investigated. The dissociation of O_2 into Ag–O clusters was promptly observed, where O atoms formed 2.2-2.3 Å bonds with the Ag atoms surrounding them. This bond length was 5~10% longer than the Ag-O bond length in crystalline Ag_2O (2.08 Å in GGA-PBE relaxed structure), and represent a reasonable increase for the liquid phase. Although Ag_2O is not thermodynamically stable under any atmosphere in molten Ag, Ag–O clusters could still contribute to the adhesion and wettability of Ag. These Ag–O clusters could be located in the bulk, at the surface of molten silver, or at the interface of the liquid-Ag and solid YSZ. Therefore, oxygen atoms were placed at these three positions and allowed to evolve using Ab Intitio Molecular Dynamics (AIMD). Figure 7 compares the initial and final structures after 3 picoseconds of AIMD simulation. The energies of the three energies minimized frames taken from the AIMD in Figure 7 suggested that the position of Ag–O clusters at the interface was the most stable, providing a work of adhesion (W_{adh}) of 0.43±0.01 J/m^2, while W_{adh} was essentially 0 J/m^2 when the Ag–O clusters were at the free surface (results not shown). Without the dissolved O_2, the pure liquid Ag had an average W_{adh} (on YSZ from GGA-PBE functional) of only 0.11±0.01 J/m^2, equivalent to a contact angle of 149° as approximated by Young's Equation. This is consistent with the experimental observation that liquid Ag does not wet YSZ [31]. Experimentally, it has been observed that the contact angle of liquid Ag decreased by 20°-35°on many oxide surfaces [32] with the addition of oxygen into the atmosphere, including a drop from 120° to 90° for Ag on YSZ [31, 33]. Here, the calculated contact angle was reduced from 149° to 111° when oxygen was present in Ag(*l*). Even with GGA-PBE functionals, which tend to overestimate the contact angles by 25° on average, the simulations were able to reproduce this ~30° decrease in contact angle with oxygen incorporation into the Ag. Hence, this work clearly showed that dissolved oxygen in Ag enhances the wettability of liquid Ag.

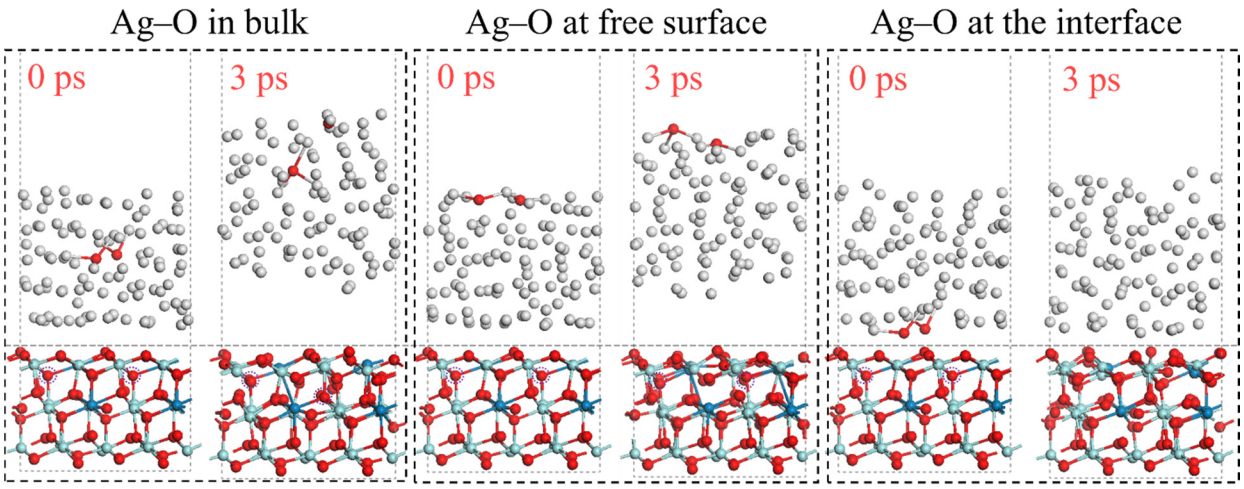

Figure 7. *Ag(l)/YSZ interface structures with dissolved oxygen atoms at the beginning and end of 3ps AIMD simulations at 1000 ˚C. Three initial positions of Ag–O clusters were investigated, including in the bulk Ag(l), at the free surface of Ag(l), and at the interface of Ag(l)/YSZ. The Ag-O at the interface is the most favorable structure.*

5.3.2 Descriptor (σ_{MO}) for Identification of Oxide Scales with High Adhesion to Ag and YSZ

DFT simulations were also performed to search for oxides that might segregate to the Ag-YSZ interface and promote Ag wetting and adhesion on YSZ. Figure 8a shows the DFT computed interface energy and its relationship with the developed descriptor σ_{MO} in various types of oxides that accounts for the density of various surface atoms. The simple descriptor enabled assessment of the interfacial oxide properties leading to high or low interfacial energy. The results plotted in Figure 8a demonstrate that the descriptor is well-correlated with the DFT calculated interface energy, which monotonically increases with the descriptor. A fitting equation,

$$\gamma_{12}^{\mathrm{pred}} = 0.55\ln(\sigma_{\mathrm{MO}}) + 2.43 \qquad \text{(Eqn. 1)}$$

was obtained with a coefficient of determination $R^2 = 0.95$. Hence, this equation was used to estimate the oxide-YSZ interface energy ($\gamma_{12}^{\mathrm{pred}}$) solely based on the descriptor. The predicted interface energy was then used to predict $W_{\mathrm{adh}}^{\mathrm{pred}}$, which is easier to measure or compute with DFT calculations.

The predicted $W_{\mathrm{adh}}^{\mathrm{pred}}$ is plotted against the DFT calculated W_{adh} in Figure 8b, which also demonstrates satisfactory accuracy. The conclusion obtained from the two ends of the W_{adh} plot indicated that ZrO_2 and YSZ were among the hardest oxides for Ag to wet. On the other hand, while both Fe_2O_3 and Rh_2O_3 provided high adhesion, like CuO, both of them are not stable under the reducing atmospheres found in SOFC anodes (Fe_2O_3 would be reduced at temperature above 587 ˚C for an atmosphere with equal partial pressures of water and hydrogen). Of the simple oxides shown in Figure 8b,the candidate with the highest W_{adh} that would be stable in a SOFC anode environment is In_2O_3, but its W_{adh} is only 1.03 J/m^2 which is 0.4 J/m^2 lower than CuO. Of the simple oxides examined, CuO was unfortunately the best for promoting Ag wetting on YSZ.

Since no new promising simple oxides were identified, the descriptor was used to search for promising multi-cation oxides. From this analysis, it was found that several oxides with a

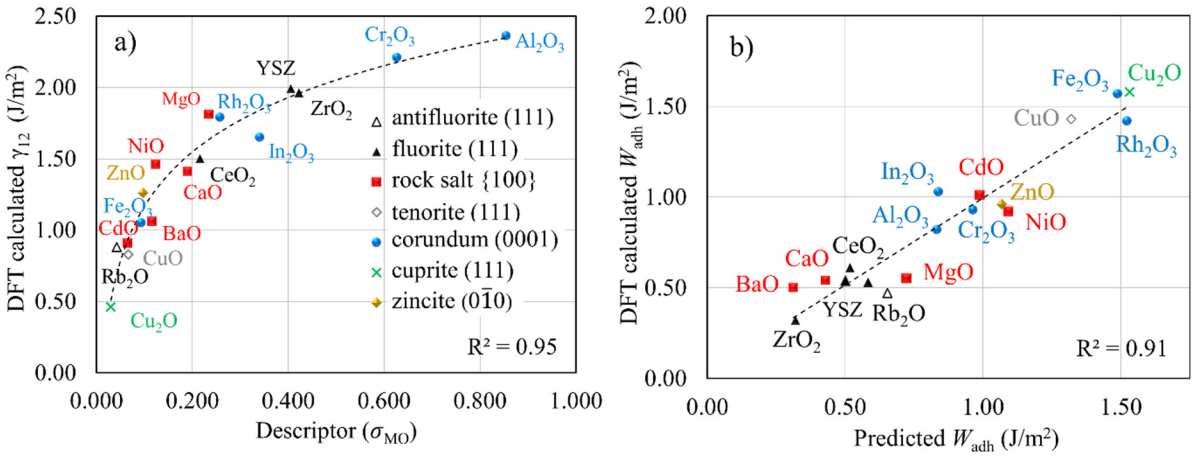

Figure 8. *The correlation a) between of the interface energy (γ_{12}^{DFT}) of Ag/oxides and the descriptor (σ_{MO}), which followed a logarithmic function, and b) between the predicted work of adhesion (W_{adh}^{pred}) at Ag/oxides interface and the DFT calculated one (W_{adh}).*

delafossite structure could exhibit strong adhesion due to their high surface energy relative to low predicted interface energy. These include (0001) surface of $CuAlO_2$, $CuGaO_2$, and $CuInO_2$, which showed a higher predicted W_{adh} (2.3~2.6 J/m^2) than Ag with CuO (1.43 J/m^2). The formation of $CuAlO_2$ would be favorable in certain conditions as the $CuAlO_2$ formation energy was calculated to be -9.70 eV, which is comparable to -9.74 eV for ½(Al_2O_3 + Cu_2O). Experimental phase diagrams indicate that $CuAlO_2$ is stable at high temperature, especially in brazing and SOFC operating temperature ranges [35]. Putting the calculated formation energy of $CuAlO_2$ on the Ellingham diagram shows that it should be stable in a SOFC anode environment. To further investigate this promising oxide and also obtain the accurate W_{adh}, DFT calculations were performed on a half-sandwich model for Ag/$CuAlO_2$ interface. The DFT-calculated W_{adh} of Ag/$CuAlO_2$ was 3.04 J/m^2, almost twice of that at the Ag/CuO interface. This high adhesion should lead to complete wetting (0°). Moreover, calculations using a half-sandwich model also indicate strong adhesion (W_{adh}= 2.04 J/m^2) between $CuAlO_2$ and YSZ. Overall, this is in accordance with reports that the greater extent of $CuAlO_2$ formed from the unintended reaction of CuO with Al_2O_3, the lower contact angle of Ag [32]. Cu_3TiO_4(010) yielded a predicted W_{adh} of 2.12 J/m^2, which is also higher than that of CuO. Cu_3TiO_4 has a similar structure to delafossite, and its (010) surface is equivalent to the (0001) surface of delafossite oxides. Also, its formation energy (-13.12 eV) in the Ellingham diagram indicates that Cu_3TiO_4 should be stable in a SOFC anode environment. IN summary, oxide interlayers of CuAl(or Ga)O_2 or Cu_3TiO_4 (which have been identified here for the first time) could improve the interfacial strength of Ag-YSZ braze joints. Unfortunately, due to time constraints, these new braze interlayers were not tested experimentally.

5.4 Transient Porous Nickel Interlayer Enabled Silver Brazing

5.4.1 CuO-Free Ag Brazes for SOFC Applications

The hypothesis of this portion of the project was that porous nickel interlayers, instead of reactive element additions, could be used to 1) promote Ag wetting on YSZ and 2) produce high-quality YSZ-stainless steel braze joints in inert atmospheres. This seemed possible for several reasons. First, although silver has a high ~1000 °C wetting angle of ~90° [8] on nickel in air

(because NiO forms on the surface in air), this drops to < 30° for $pO_2 < 10^{-9}$ atm [9]. This reduced wetting angle should make Type I pores (i.e. manufacturing pores resulting from the high ~45° wetting angle for Ag-3CuO on YSZ [10, 11]) much less likely. Second, since spontaneous liquid infiltration into porous solid media occurs for wetting angles below 51° [12], brazing with a porous nickel interlayer should bring the Ag into intimate contact with the YSZ, lowering the likelihood of Type I pore formation. Third, the high 1455 °C melting point of Ni [13], the low 962 °C melting point of Ag [13], and the low, ~1 % 1000°C solubility of Ni in Ag [13] should ensure that a solid, porous nickel network remains present long enough to bring silver into contact with the YSZ. Fourth, because commonly used SOFC cathode materials, such as $La_{0.6}Sr_{0.4}Co_{0.2}Fe_{0.8}O_{3-x}$ (LSCF) and $La_{0.6}Sr_{0.4}MnO_{3-x}$ (LSM), are thermodynamically stable down to a pO_2 ~10^{-12} atm at ~1000 °C and kinetically stabilized for a few hours at even lower oxygen partial pressures [14, 15], it should be possible to braze cathode-containing SOFCs for short times in inert atmospheres without decomposing them [16]. Lastly, and perhaps most importantly, the nickel will be protected from oxidation during inert atmosphere brazing by 1) the decomposition of carbon-containing nickel paste organic additives during porous nickel interlayer production (carbon sets the local 850 °C pO_2 at ~10^{-17} atm [16] even though the incoming inert atmosphere will have a pO_2 ~10^{-6} atm), and 2) stainless steel chromium oxidation (which sets the local pO_2 even lower [16]) during brazing as molten silver infiltrates the porous nickel interlayer. Hence, since NiO will not form at 1000 °C in carbon gettered argon brazing atmospheres [16], allowing Ag-Ni joints to be free of Type II pores (the pores forming from the reduction of a metal oxide by the anode gas).

Conversely, several factors could prevent porous nickel interlayers from enabling the production of high-quality YSZ-stainless steel braze joints. For instance, Ni additions could degrade the braze interface strengths because the stress induced by swelling resulting from nickel oxidation on the cathode side of the braze joint (enabled by oxygen diffusion through silver) could nucleate cracks in the joint. Hence, to investigate the feasibility of producing high quality porous-nickel-interlayer-enabled YSZ-SS SOFC braze joints, the microstructure, chemistry, and mechanical strength of these braze joints both before and after 500 hours of 750 °C oxidation in air were evaluated. In addition, accelerated dual atmosphere thermal cycling tests were also performed.

5.4.2 As-brazed Microstructure

Figure 9 shows back-scattered electron images of the partially sintered nickel interlayers, indicating that laterally uniform, porous layers ~20 μm (2-6 Ni particles in thickness) were produced. These porous nickel interlayers were produced on YSZ supports in two steps. First, nickel paste was produced by hand-mixing 99.9% pure nickel powder that had an average particle size of 3-7 μm (Alfa Aesar Inc.) with a V-737 organic vehicle (Hereaus, Inc.) in a 2:1 ratio by weight. The nickel paste was then screen printed onto 25 mm × 25 mm YSZ|NiO-YSZ substrates. Two passes were used to print each layer, and 10 minutes of 80 °C drying was used between prints. Second, in 20 sccm of Ar, the samples were ramped at 5 °C/min, held at ~850 °C for 2 hours, and cooled to room temperature with a 5 °C /min nominal cooling rate to produce partially sintered nickel layers (denoted as the Ni|YSZ|NiO-YSZ substrate). Braze joints were produced by sandwiching a 75 μm thick, ~6.3 mm × 6.3 mm piece of 99.95% pure silver foil (Alfa Aesar Inc.) between the Ni|YSZ|NiO-YSZ substrate and a bare 441 stainless steel sheet (AK Steel Corp.), and then ramping the joint assemblies at 5 °C/min, holding at ~1000 °C for either 15 or 30 minutes, and ramping back to room temperature with a 5 °C /min nominal rate in 20 sccm of Ar.

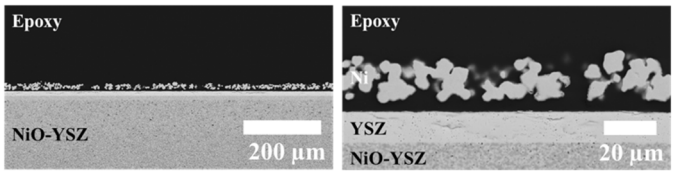

Figure 9. *Representative backscattered electron images of the partially sintered porous Ni interlayer at different magnifications.*

Figure 10 shows that both 15 and 30 minutes of brazing at ~1000 °C in Ar were sufficient to produce pore-free, laterally-uniform braze joints. Specifically, Figures 10a and 10b indicate that both brazing conditions were sufficiently long to allow Ag to spontaneously infiltrate the porous nickel interlayers and wet/spread across the YSZ and stainless steel layers. As shown in the higher magnification images in Figures 10c-e, the porous nickel interlayer layer originally located at the braze-YSZ interface largely disappeared during 15 minutes of brazing (some remnants of this layer can be seen "floating" in the middle of the silver braze joint in Figures 10a and 10c), and a new reaction layer formed at the braze-SS interface. As shown in Figures 10f-h, 30 minutes of brazing resulted in the complete elimination of the porous nickel interlayer from the braze-YSZ interface and a correspondingly thicker reaction layer. In both cases, the silver remained well-bonded to the YSZ even after the porous nickel layer disappeared. Figures 10c-g also show that residual SS surface oxides present along the SS-reaction layer interface (black dots) did not adversely affect brazing. In fact, the change in SS contrast above the line of residual surface oxides denoting the original SS-Ag boundary suggests significant intermixing and a strong metallurgical bond between the SS and the reaction layer. (Note, joints produced with identical procedures but brazed in air showed inadequate wetting of silver wetting due to nickel oxidation.)

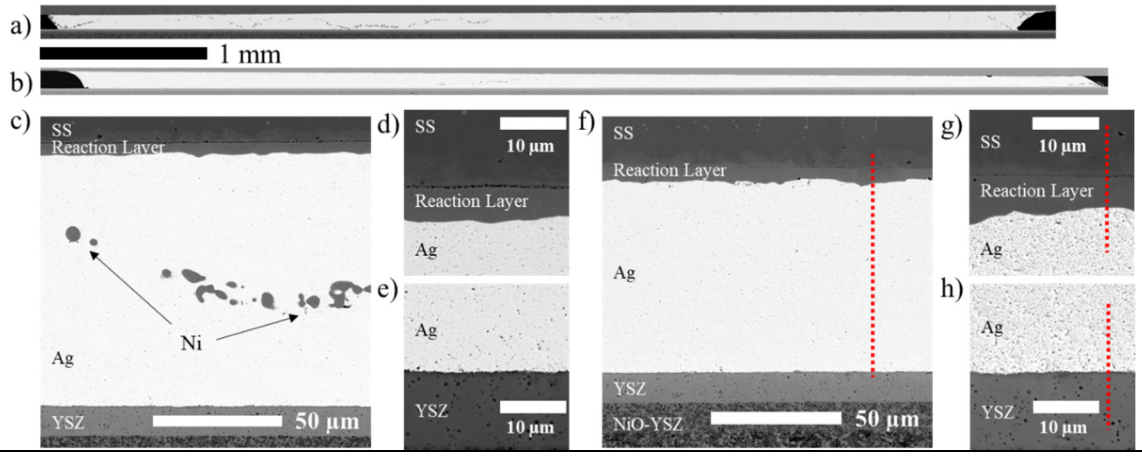

Figure 10. *Representative backscattered electron images of a) an entire 15 minutes brazed joint cross-section, b) an entire 30 minute brazed joint cross-section, c-e) zoomed-in, representative portions of the 15 minutes brazed joint, and f-h) zoomed-in, representative portions of the 15 minutes brazed joint. Note, the red dotted lines indicate the paths of the Figure 11 Energy Dispersive X-ray Spectroscopy line scans.*

5.4.3 As-brazed Joint Compositions

Figures 11a-c shows results of 30 minute brazed joint EDX compositional analyses collected along the red dotted lines in Figures 10f-h, respectively. As shown in Figures 11a and 10f, most of the as-produced braze joint consisted of "pure" silver, consistent with the low solubility of nickel, iron, and chromium in silver [13, 17]. Hence, these Ni-Ag braze joints were expected to benefit from the conveniently large ductility of silver. This high ductility provides a stress-relief mechanism that allows YSZ-SS braze joints made with Ag-Cu brazes to survive for extended thermal cycling [18, 19] despite the fact that YSZ, 441 SS, and silver have very different 25-1000ºC thermal expansion coefficients of ~8.9-10.6 [20], ~9.3-13.5 [21], and ~15-25 [22] ppm/K, respectively.

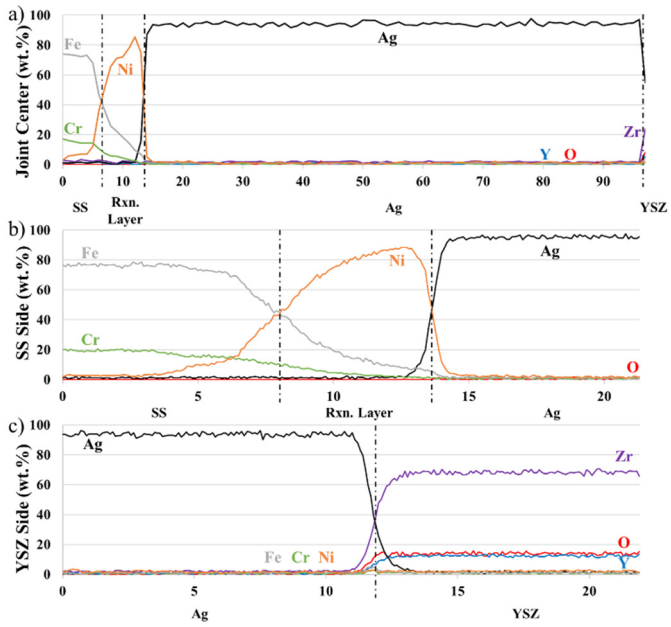

Figure 11. *Representative Energy Dispersive X-ray Spectroscopy line scan results from the 30 minute as-brazed sample a) across the joint center, b) across the SS-braze interface, and c) across the YSZ-braze interface at the locations indicated in Figure 10. Note, the x-axis is in microns.*

Figure 11b shows that the braze-SS reaction layer consisted of relocated nickel from the porous interlayer and diffused Fe and Cr from the SS. The lack of discrete nickel particles within a silver matrix in the reaction layer, the fact that samples brazed upside down (i.e. the lower pairs of double shear lap sample joints) formed the same microstructure as that shown in Figure 10, and the presence of nickel interlayer remnants in the Figures 10a and 10c braze interiors suggested that both atomic diffusion and convective transport assisted in the disintegration or dissolution of the porous nickel interlayer and the formation of the reaction layer. Figures 11a-b also show good nickel, iron, and chromium inter-diffusion across the SS-reaction layer interface, suggesting a strong metallurgical bond between these layers.

Figure 11c shows that a compositionally "sharp" Ag-YSZ interface resulted after removal of the porous nickel interlayer. It is important to note that the "diffusion distance" implied by the apparent gradual transitions of the Ag, Y, Zr, and O content across the transition was equal to the ~3 micron estimated EDX electron beam interaction volume diameter and therefore cannot be interpreted as intermixing of Ag and YSZ (the intermixing distances in Figure 11b are much larger than 3 microns and hence represent true intermixing between the SS and the reaction layer). Similarly "sharp" Ag-YSZ compositional interfaces have been observed in other silver-YSZ brazing systems [23].

5.4.4 Post-oxidation Braze Joint Microstructure

Figure 12 shows the 30 minute brazed joint microstructure after 120 and 500 hours of 750 °C oxidation in air, respectively. In both cases, the braze joints remained solid and dense after

oxidation and the braze remained bonded to both the SS and the YSZ. Further, the majority of the braze joint, which consisted of pure silver, was microstructurally unaffected by the 750 °C exposure to air. The lateral continuity of the Figure 12a and 11b braze joint microstructures, and the similarities between the 120 and 500 hour oxidized braze joint microstructures suggests that 120 hours was plenty of time for oxygen to diffuse into all portions of the braze joint.

Figures 12b, 12c, 12f, and 12g show that the Ni-rich portion of the reaction layer oxidized and formed two distinct layers, each with reduced porosity with increasing oxidation time. This is consistent with 1) the fact that pure Ni oxidizes quickly in 750 °C air [16, 24], 2) the fact that Ag has a high oxygen ion conductivity of 1.5×10^{-5} $cm^2 \cdot s$ at 750 °C, and 3) the fact that the Ni-rich portion of the reaction layer was adjacent to the thick silver layer at the interior of the braze joint. These figures also show that the Fe and Cr rich portion of the reaction layer (which extends past the line of residual surface oxide particles and up into the SS) did not oxidize, and that a thin silver layer (denoted Ag*) often separated the oxidized and unoxidized portion of the reaction layer. Given the high ductility of pure Ag [25], it is likely that this Ag* layer formed from the volume expansion associated with oxidation of the nickel-rich portion of the reaction layer (the atomic volumes of iron oxide, nickel oxide, and chromium oxide are greater than that of their constituent cations [24]).

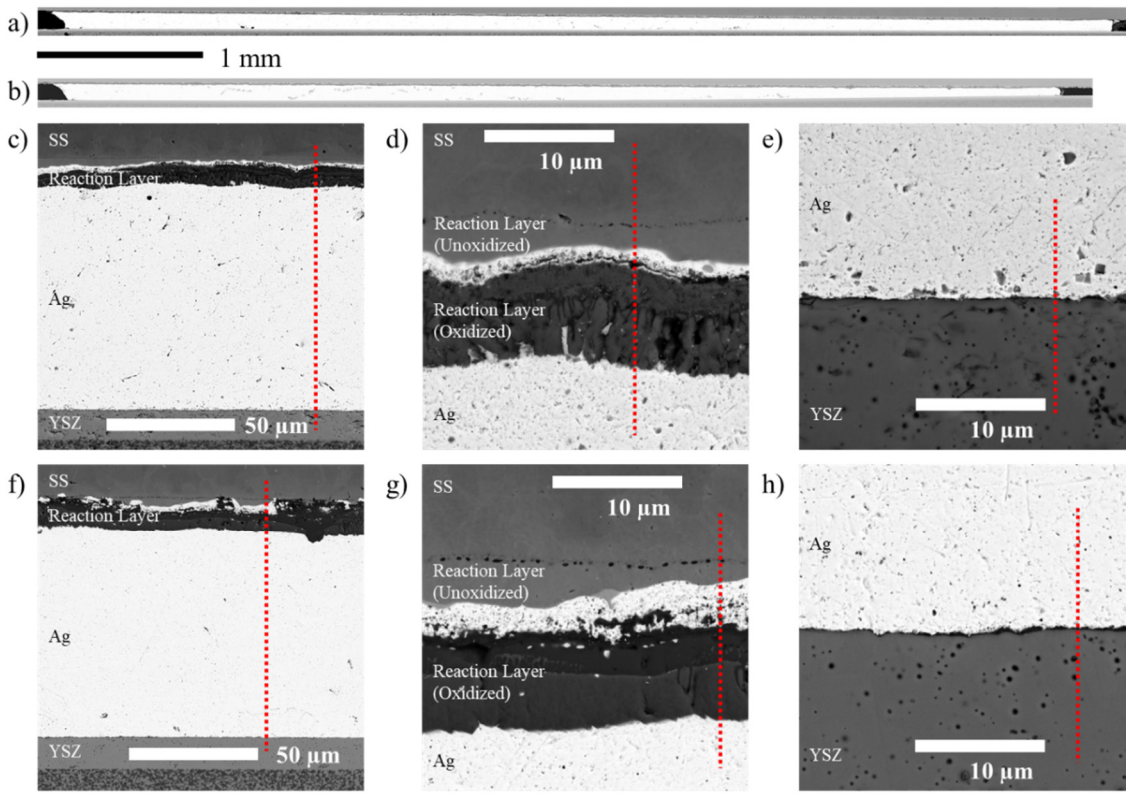

Figure 12. *Representative backscattered electron images of a) an entire 120 hour 750 °C oxidized braze joint cross-section, b) an entire 500 hour 750 °C oxidized braze joint cross-section, c-e) higher magnification representative portions of the 120 hour 750 °C oxidized braze joint, and f-h) zoomed-in, representative portions of the 500 hour 750 °C oxidized braze joint. Note, the red dotted lines indicate the paths of the Figure 13 Energy Dispersive X-ray Spectroscopy line scans. Both samples were initially brazed for 30 minutes.*

Figures 12e and 12h show that except for a thin dark phase forming at the interface, the oxidized braze-YSZ interface microstructure did not change with long-term 750 °C oxidation.

5.4.5 Post-oxidation Braze Joint Compositional Analysis

Figures 13a-f show results of 30 minute brazed joint EDX compositional analyses collected along the red dotted lines shown in Figures 12c-h, respectively.

Consistent with the SEM contrast in Figure 12, Figures 13a and 13d show that the center of the braze joint remained pure silver after 120 and 500 hours of 750 °C oxidation. Figures 13b and 13e clearly show the Ag* layer, the unoxidized reaction layer, and (especially in Figure 13e) two different phases within the oxidized portion of the reaction layer. These figures also show that a chromia-rich layer (denoted by the green highlighting) formed between the Ag* and oxidized reaction layer. Given chromia's excellent surface passivation characteristics at 750 °C in other systems [26, 27], this chromia layer likely helped protect the unoxidized portion of the reaction layer from the oxygen conducted through the silver in the center of the braze joint, providing a diffusion barrier that at least partially protects the SS from oxidation.

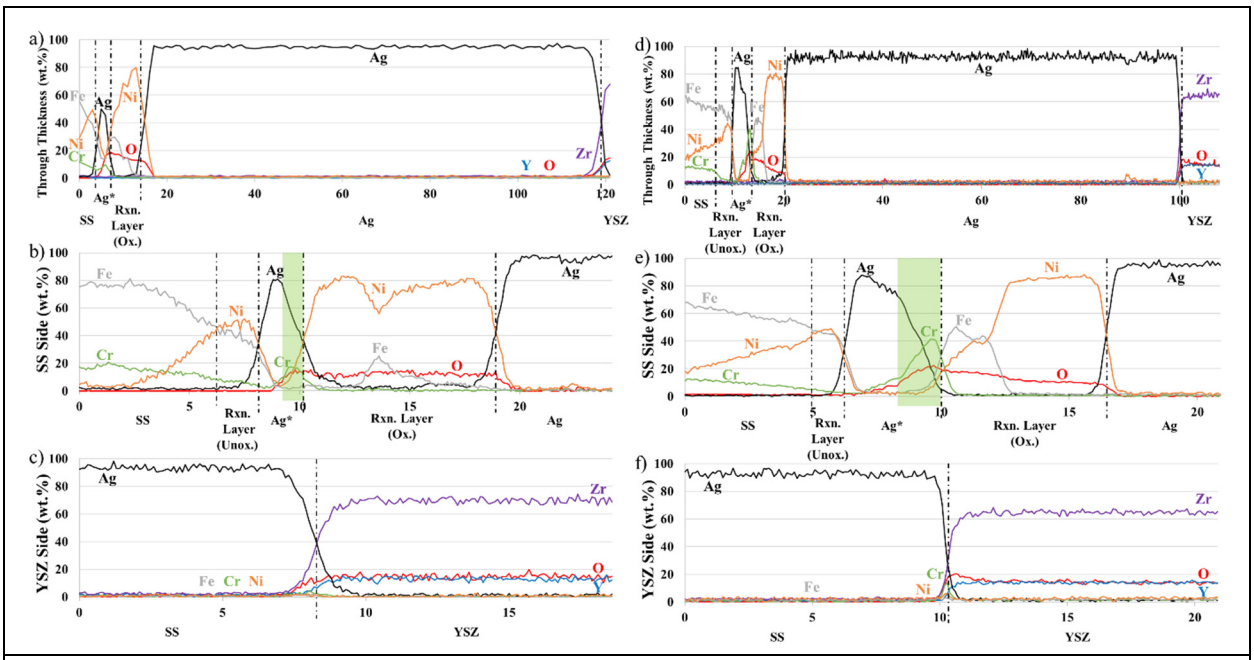

Figure 13. *Representative Energy Dispersive X-ray Spectroscopy line scan results from a 30 minute brazed sample a) across the 120 hour 750 °C oxidized joint center, b) across the 120 hour 750 °C oxidized SS-braze interface c) across the 120 hour 750 °C oxidized YSZ-braze interface, d) across the 500 hour 750 °C oxidized joint center, e) across the 500 hour 750 °C oxidized SS-braze interface f) across the 500 hour 750 °C oxidized YSZ-braze interface. Note, the x-axis is in microns.*

Like the as-produced braze joint EDX analysis of Figure 11c, the 120 hour oxidized sample EDX analysis of Figure 13c shows a "sharp" interface between the braze and the YSZ. However, as shown in Figure 13f, longer oxidation times resulted in detectable amounts of nickel oxide and chromium oxide at the braze-YSZ interface. These phases likely correspond to the dark phase seen along the braze-YSZ interface in Figure 12h (and to a lesser extent Figure 12d). In light of the poor wetting characteristics of Ag on YSZ [28] and the low predicted work of adhesion for Ag

on YSZ [29], the higher work of adhesion predicted between Ag and nickel, nickel oxide, or chromium oxide on the surface on YSZ [29], it is likely that small amounts of residual nickel from the porous nickel layer and chrome that diffused through the Ag may have oxidized in the interface to the braze-YSZ interface and also helped prevent Ag dewetting after dissolution of the porous nickel interlayer.

Figure 14 displays EDX composition maps showing the lateral continuity of the various braze joint layers with the same trends as the Figure 13 line-scan.

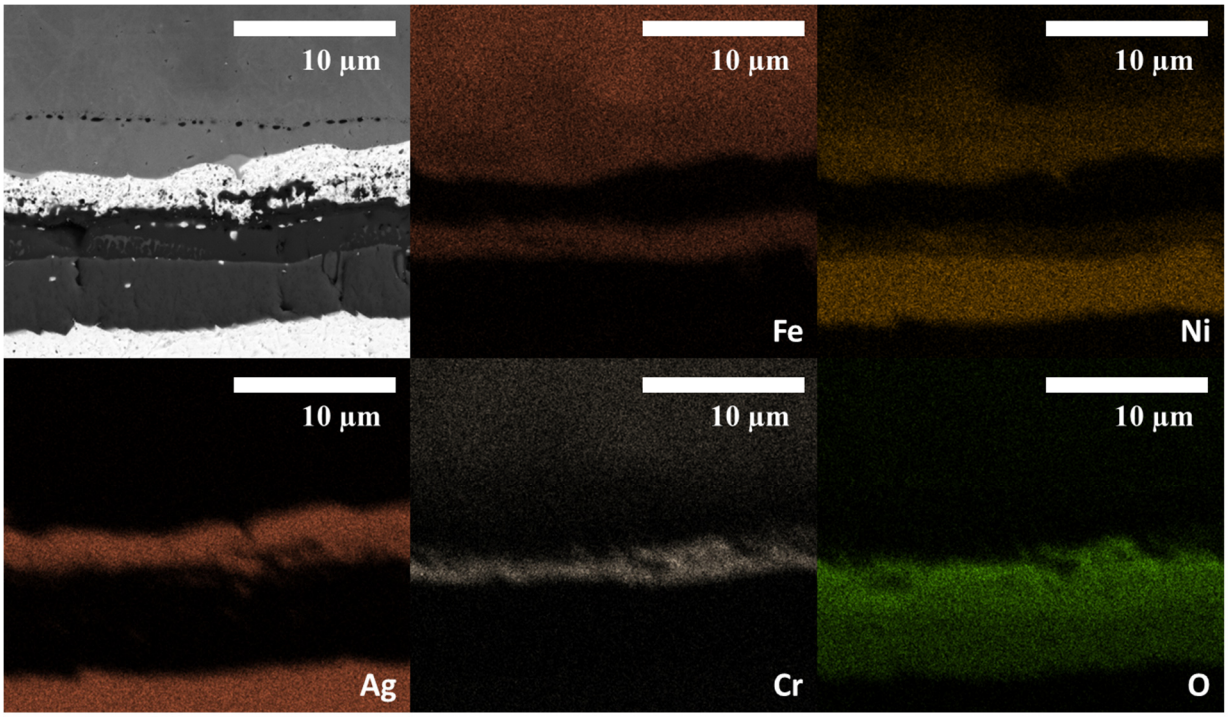

Figure 14. *Braze-SS interface element distribution maps for a representative 30 minutes brazed sample after 500 hours of 750°C oxidation. The top left picture is the backscattered electron image of the mapped area.*

5.4.6 Braze Joint Mechanical Tests

As shown in Figures 15a and 15b, a symmetric double shear lap geometry was used to test the shear strength of the as-produced and oxidation-tested braze joints using a mechanical tensile test machine (SFM-20, United Testing Systems, Inc.). Each double shear lap sample contained four 0.635 cm × 0.635 cm square brazed joints (two on each side). As shown in Figure 15c, an extensometer was fixed on both stainless steel plates to measure the real extension in the braze regions,

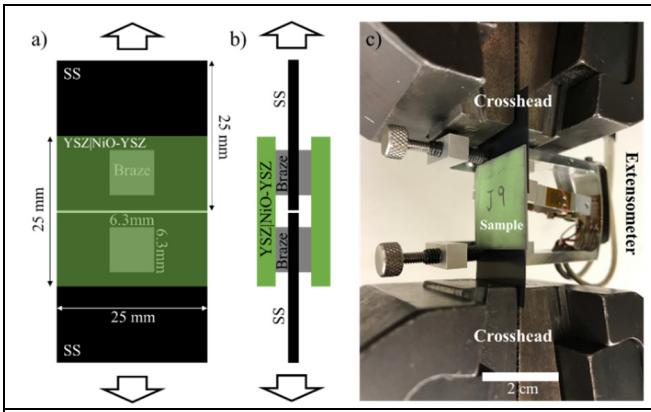

Figure 15. *a) A front-view schematic, b) a side-view schematic, and c) picture of the symmetric double shear lap samples used here for mechanical testing.*

and all samples were tested to failure at room temperature with displacement rate of 0.009 mm/min. The shear stress σshear and strain εshear were estimated using the equations:

$$\sigma_{shear} = F/2[a\times(a-\delta)] \quad (1)$$

$$\varepsilon_{shear} = (\delta/2)/t \quad (2)$$

where F was the load; a was the lateral length of the joints (here 0.635 cm); δ was the extension; and t was the joint thickness (here ~100 μm) [30]. A double shear lap geometry, which restricts rotational loading on each braze joint through its symmetrical design, placed each braze joint in a simple shear loading geometry that resembled the coefficient-of-thermal-expansion-mismatch induced loading conditions present in a planar SOFC braze joint.

Figure 16 shows room temperature stress-strain curves for the SS|Ni-Ag|YSZ braze joints after 1000 °C fabrication in Ar, 120 hours of 750 °C oxidation, and 500 hours of 750 °C oxidation. In all cases the braze joints exhibited large amounts of deformation (>30% of shear strain) before failure, and when failure did occur it always occurred with the brittle fracture of the underlying YSZ|NiO-YSZ supports and not through braze or braze interface. Kuhn *et al.* have observed similar cracking within the YSZ supports in their SS|Ag|YSZ brazes [28]. In addition, other studies have shown similar SS-Ag-YSZ failure mechanisms to those reported here [30, 31]. Despite the variations in the shape of the curves, which was probably due to lateral braze joint thickness variations (such as those in Figures 10a-b) caused by the somewhat crude experimental setup here, both sets of samples showed good reproducibility. The decreasing failure strain with increasing oxidation shown in Figure 16 is indicative of a loss of ductility, or a reduction in the effective braze joint thickness, with oxidation (and hence earlier load transfer to the YSZ|NiO-YSZ substrate). However, the fact that much of the joint will remain unoxidized in a real SOFC application (due to the pO_2 gradient extending laterally across the joint and the low oxygen partial pressure set on the fuel side of the joint) and the large > 30% failure strains observed here for the heavily oxidized portion of the joint after 500 hours, suggested that these SS|Ni-Ag|YSZ braze joints will likely remain mechanically robust over SOFC lifetimes. In addition, shorter brazing times closer to the 1-5 minutes reported in the literature [32] may be able to increase joint longevity by keeping the remnants of the porous nickel interlayer within the middle of the joint so that Ni can oxidize "freely" in "all" directions into a ductile silver matrix.

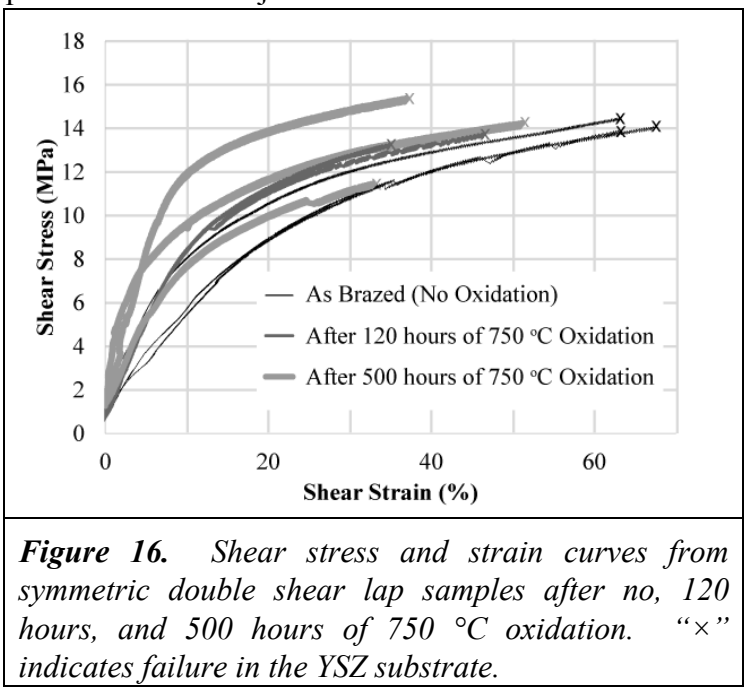

Figure 16. *Shear stress and strain curves from symmetric double shear lap samples after no, 120 hours, and 500 hours of 750 °C oxidation. "×" indicates failure in the YSZ substrate.*

5.4.7 Summary

A new transient porous-nickel enabled silver-based braze for improved YSZ-to-stainless steel joining was developed, and it may also serve as a design paradigm to enable silver (or other

braze) to ceramic sealing in automotive, aerospace, and other joining applications. Like reactive air brazing, the current brazing technique can be performed in atmospheres (i.e. inert atmospheres) that do not degrade the mechanical and electrochemical performance of pO_2 sensitive SOFC electrode (such as LSCF) or electrolyte (such as ceria) materials. As summarized in Table 5, this technique reduces the porosity commonly found in the conventional YSZ-stainless steel braze joints produced using reactive air brazing (Ag-CuO), and the likelihood of enhanced lifetimes and operational robustness in SOFC braze joints appears to be likely.

Table 5 Comparison of Conventional Reactive Air vs. Porous-Nickel-Enabled Ag Brazing.

Pore Type	Reactive Air Brazing	Ag-Ni Brazing
Type I (wetting) Pore Formation	• $\theta \approx 45°$ (for Ag-4CuO) occasionally leads to pores during manufacturing [10, 11] • Organics in the braze paste can also lead to pores during manufacturing [33]	• $\theta = 30°$ leading to a fully infiltrated porous Ni network [8, 9, 12] • Since no organics are used during brazing (these are removed by heating the nickel paste in Ar to obtain the porous nickel network) binder burnout cannot cause pores during brazing
Type II (interfacial) Pore Formation	• With the reduction of CuO along the braze/YSZ and braze/SS interface, micro-pores will form during SOFC operation near the H_2 side of the joint [18, 19].	• Even after 500 hours of oxidation no oxides are present at the SS-braze interface on the anode side of the joint (the oxides forming from the reaction layer are within ductile silver, and only form on the air side of the joint), hence they cannot be reduced by anode gases to produce pores.
Type III (H_2+O_2) Pore Formation	• H_2 and O_2 diffuse through Ag and form water pockets (Type III pores) that mechanically compromise the braze joint after ~10,000 hours of SOFC operation [34].	• Since Type II pores form much faster than Type III pores [18, 35] and thereby provide a short-circuit path for H_2 invasion into the center of the braze, the elimination of Type II pores should increase joint reliability by delaying the onset of Type III pores.

5.5 Dual Atmosphere Reliability of Ag-Ni Brazes

Dual atmosphere isothermal aging (DAI) tests and dual atmosphere accelerated thermal cycling tests (DAATC) on both Ag-CuO and Ag-Ni SS to YSZ braze joints were also conducted. A testing geometry was developed for both DAI and DAATC tests using samples with the novel Ag-Ni brazing method as well as the of conventional RAB (Ag3CuO, mol.%) braze joints for comparison. The DAI tests were designed to evaluate the interfacial damage caused by Type II porosity formation. Considering the large differences in the 25-1000 °C coefficients of thermal expansion in YSZ, 441 SS, and silver (~8.9-10.6 [20], ~9.3-13.5 [21], and ~15-25 [22] ppm/K, respectively), high levels of shear stress will be imposed on the braze interfaces during thermal cycling. The DAATC tests were designed to assess the combined effects from thermal-mechanical loadings and chemical reactions from the dual atmosphere temperature cycles.

5.5.1 Dual Atmosphere Test Set-up

As shown in Figure 17, the as-fabricated 3-layer (SS, braze, YSZ|NiO-YSZ) ring samples were stacked up with a mica ring between each sample; then the whole stack was screwed tight between two thick SS plates (Figure 17a bottom). As shown in Figure 17b, the assembly was placed on top of the gas inlet tube with a block of SS cylinder piece on top. To achieve dual atmosphere conditions, a 300 sccm flow 4% H_2 96% N_2 through a distill water bubbler was sent through the gas inlet at the bottom of the stack, creating a reducing atmosphere near the center of the ring samples (denoted as the 'RE' side); whereas the outer rim of the braze region was exposed to an oxidizing atmosphere (denoted as the 'OX' side) by exposing the entire stack to air. The SS piece on top of the stack would help decrease the out-gassing rate and maintain a slight positive pressure in the center gas stream. Also, there is an 'exterior thermocouple' ('External Temperature') attached to the top SS plate (Figure 17b) as well as an interior thermocouple ('Inlet Temperature') at the gas inlet next to the bottom SS plate. These thermocouples monitored the sample temperatures throughout the tests. For the dual atmosphere isothermal (DAI) test, the entire assembly was sent up into a three-zone furnace to keep both the inlet temperature and external temperature at 755±5 °C for 310 hours.

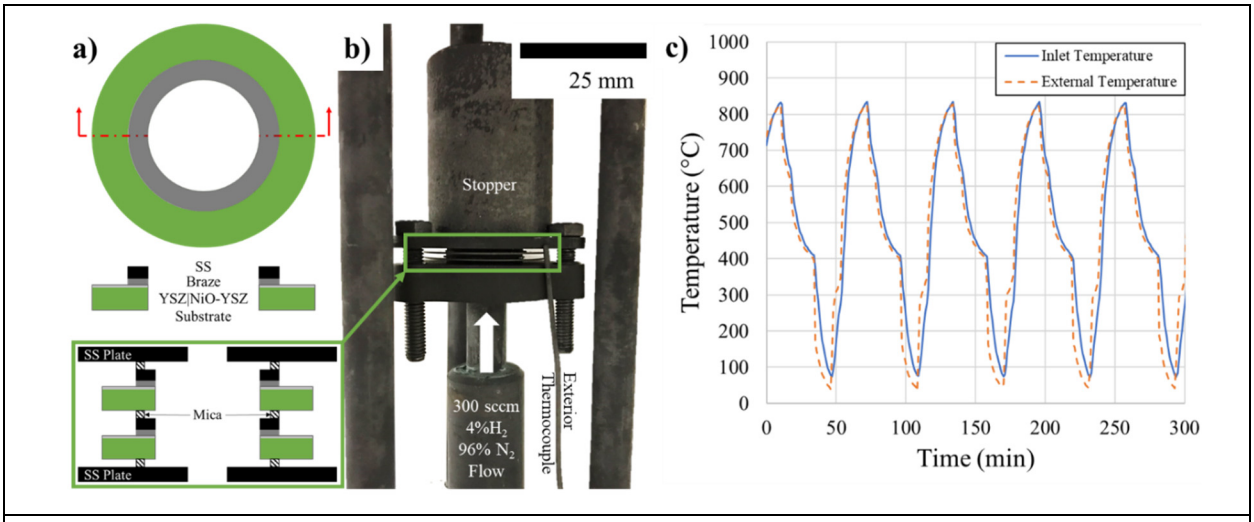

Figure 17*. a) Schematic diagrams of sample geometry and stack arrangement in the test set-up (note that the thicknesses of the components are exaggerated); b) Picture of the test set-up where the sample is cycled in and out of the three-zone furnace; c) Recorded inlet and external temperature of the test stack during dual atmosphere thermal cycling.*

5.5.2 As-brazed RAB Microstructure

Figure 18a shows that a relatively dense joint was obtained with Ag-3CuO RAB material. There is a big pore reaching both the SS and YSZ interface at the middle of the joint, which is a common characteristic of RAB brazing related to its mildly high wetting angle on YSZ and/or organics within the RAB paste [10, 11, 32, 33, 36-43]. The labels 'OX' and 'RE' in Figure 18a indicates the sides of the sample subjected to oxidizing (air) and reducing (4% H_2 96% N_2) environments in the subsequent tests, respectively.

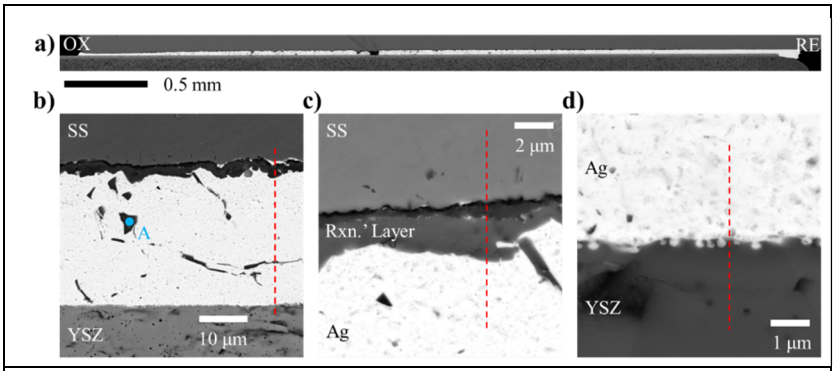

Figure 18. *Representative BSE images of a) an entire as-brazed Ag-3CuO joint cross-section, zoomed-in, representative portions of the joint microstructure b) through thickness, c) at the SS interface, and d) at the YSZ interface. Note, the red dotted lines indicate the paths of the Figure 19 EDX line scans.*

Figure 18b shows the through-thickness microstructure of the Ag-3CuO braze joint between 441 SS and YSZ|NiO-YSZ, which was representative of the microstructure between the OX and RE sides in Figure 18a. The EDX line scan results from the red dotted lines in Figure 18 are presented in Figure 19. It is obvious from Figure 18b and Figure 19a that the bulk of the braze joint consisted of pure silver with the lightest contrast, and that the phase within the bulk silver in the middle (vertical) of the joint was a Cu-Cr-O oxide (also confirmed at dot 'A' by EDX point scan). There was also formation of a reaction layer (denoted as the "reaction' layer" or "rxn' layer" hereafter) at the SS interface that was typical of RAB joints made between SS and ceramic substrates [28, 41, 44].

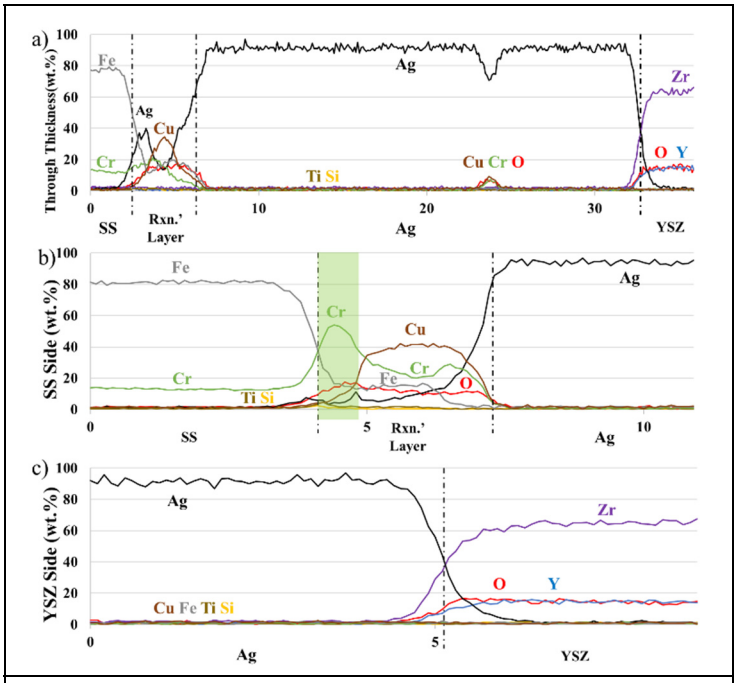

Figure 19. *Representative EDX line scan results from the 30 minute as-brazed Ag-3CuO sample a) across the joint center, b) across the SS-braze interface, and c) across the YSZ-braze interface at the locations indicated in Figure 18b-17d, respectively. Note, the x-axis is in microns.*

Figure 18c shows a zoomed-in view of the reaction' layer at the SS interface. The contrast difference within the reaction' layer indicates that it consisted of two parts. Figure 19b shows the EDX line scan results, and it is obvious that the layer with the darker contrast closer to the SS was a high-Cr containing oxide layer, probably chromia; and the layer with the lighter

contrast closer to the bulk silver portion was a Cu-Cr-Fe-O layer. This phase distribution was very similar to other studies where a reaction' layer consisting of Cr-O and Cu-Fe-Cr-Mn-O layers is observed in Crofer/RAB/ceramic joints [28, 41, 44, 45].

Figure 18d shows the typical as-brazed RAB microstructure at the YSZ interface. A thin layer (<300 nm) can be observed between silver and YSZ at the interface. This layer was probably CuO that decorates the YSZ surface for improved silver wetting [10, 44]. However, the CuO layer was not detected by the EDX line scan in Figure 3c, probably due to its small thickness.

5.5.3 Ag-3CuO Braze Joints

Figure 20a shows a BSE image of the entire cross-section of a 300 hour DAI tested Ag-3CuO braze joint, while Figure 20b shows zoomed-in images at the areas indicated by the blue arrows in Figure 20a, respectively. Compared to the as-brazed Ag-3CuO microstructure in Figure 18a, it is obvious that significant amount of porosity developed along the SS interface within the reaction' layer during dual atmosphere isothermal aging. The pores which developed in the middle of joint toward the RE side were larger in size, larger in quantity, and more percolated than the pores that developed toward the OX side. This was consistent with the fact that the major pore formation mechanism is the reduction of CuO by H_2 from the RE side of the joint [18, 30, 35, 41] (Type II reduction pores). Another feature of these Type II pores is that the porosity was mostly concentrated within the reaction' layer and closer to the silver portion (vertically) of the braze joint. This was because the Cu-rich oxides in the reaction' layer (that were reduced to cause the pores) were originally distributed toward the silver phase, as discussed previously (Figure 18c). Other studies [19, 41] have also made the same observations in samples exposed to dual atmosphere environments.

Figures 20c-d show the typical zoomed-in Ag-3CuO braze microstructure after 300 hour DAI testing. Except for the porosity developed, the braze microstructure after the DAI test in Figure 20c was very similar to that in the as-brazed condition. This was reasonable since 1) the 441 SS, the reaction' layer, the silver phase, and the YSZ|NiO-YSZ substrate were almost immune to oxidation, and 2) only Cu-rich oxides within the reaction' layer were reduced by H_2 from the RE side. Similar observations at both the SS interface (Figure 20d) and the YSZ interface (Figure 20e) have confirmed this finding. Similar results were also observed on the 300 cycles DAATC tested Ag-3CuO braze joints. After the DAATC tests, significant porosity developed across the SS/braze interface in these conventional Ag-CuO RAB joints (data not shown).

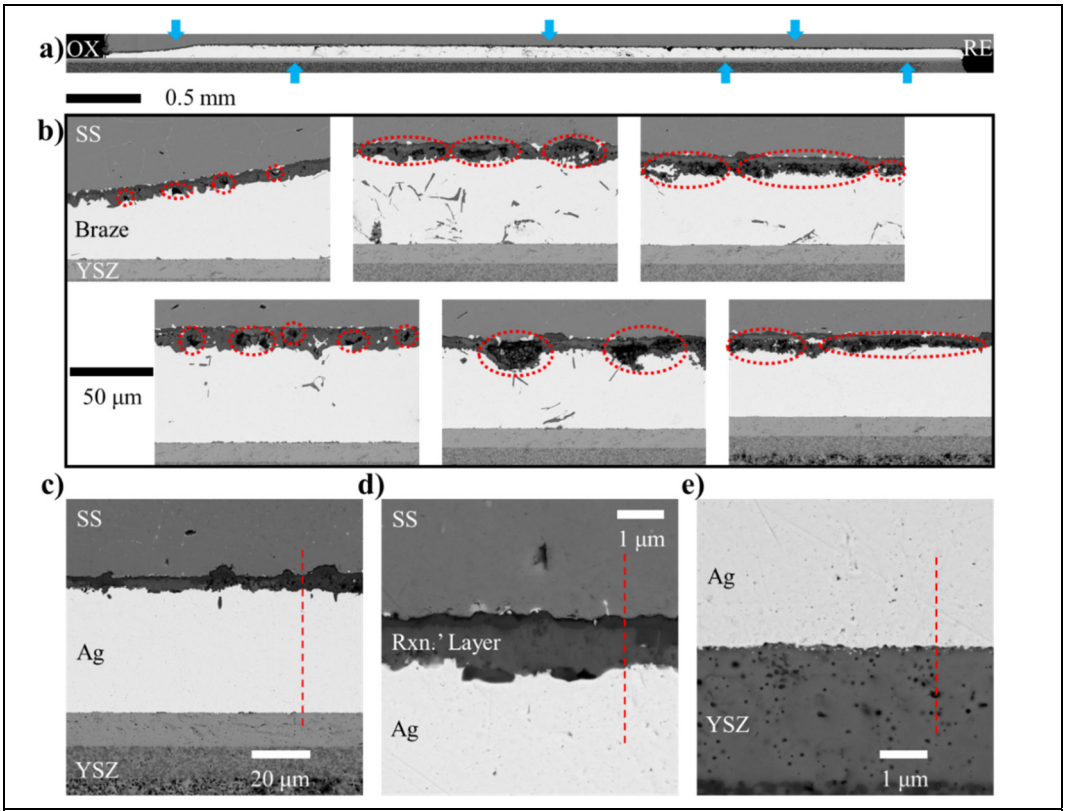

Figure 20. *Representative BSE images of a) an entire 300 hour DAI tested Ag-3CuO braze joint cross-section; b) a series of zoomed-in images of the areas marked by the blue arrows; and zoomed-in, representative portions the joint microstructure c) through thickness, d) at the SS interface, and e) at the YSZ.*

5.5.4 Ag-Ni Braze Joints

Figure 21a shows a BSE image of the entire cross-section of a 300 hour DAI tested Ag-Ni braze joint. Figure 21b and 20c provide zoomed-in views of this layer at the OX side. This microstructure was very similar to the results from the air-oxidized Ag-Ni samples in Figure 12. The OX side was exposed to air at the same temperature (~750 °C) for 300 hours during the DAI test, and it showed features with an intermediate level of oxidation between the 120 hour and 500 hour oxidized microstructures Figure 12. The original Ag-Ni braze reaction layer was partially oxidized, became micro-/nano-porous, and separated from the unoxidized reaction layer, creating a layer of silver in between (denoted as the Ag* layer), as seen in Figure 12. Figure 22a shows the EDX line scan results from Figure 21b. Compared to the as-brazed condition, there is no change to the bulk silver whereas most of the changes occurred within the reaction layer. Figure 21c further shows that layered features can be observed both below the Ag* layer (with a continuous dark contrast) and within the oxidized reaction layer. EDX line scan results in Figure 22b show that a protective chromia layer (green shade) formed within the Ag* layer next to the oxidized reaction layer; and that the compositional distribution within the oxidized reaction layer shows a layer of Ni, Fe oxides with Ag 'scrambled' in between. It should be noted that the black phase appearing as a layer between the SS and the unoxidized reaction layer is the pre-brazing surface oxide scale from the SS.

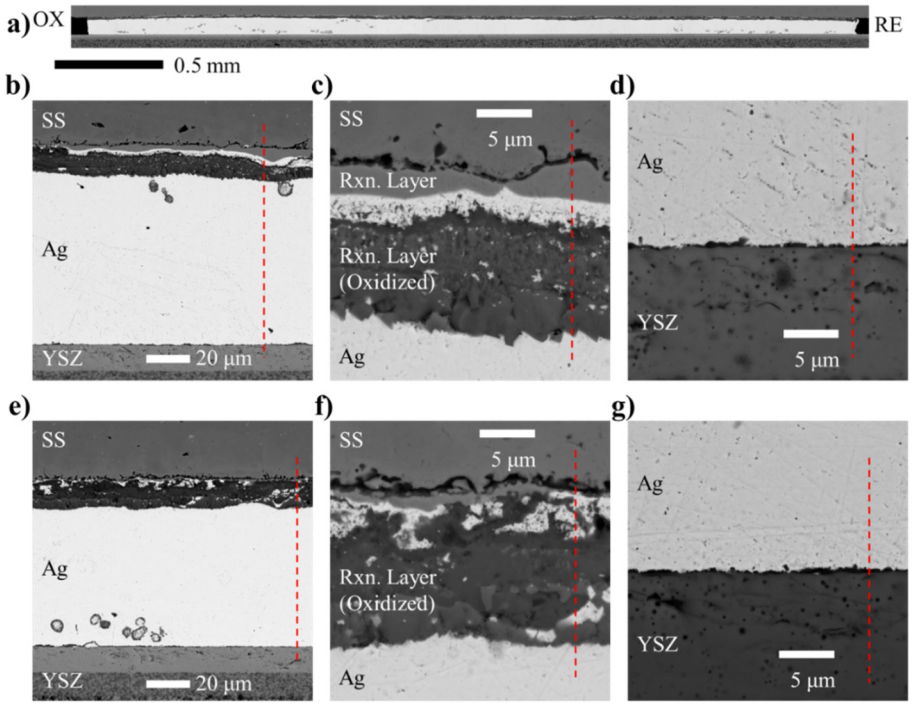

Figure 21. *Representative BSE images of a) an entire 300 hour DAI tested Ag-Ni braze joint cross-section; and zoomed-in images at the OX side showing the microstructure b) through thickness, c) at the SS interface, and d) at the YSZinterface; as well as zoomed-in images at the RE side showing the microstructure e) through thickness, f) at the SS interface, and g) at the YSZ interface. Note, the red dotted lines indicate the paths of the Figure 22 EDX line scans.*

Figure 21e shows the through thickness microstructure of the 300 hour DAI test Ag-Ni sample at the RE side. Compare to Figure 21b, the Ag* layer was no longer continuous, and the oxidized reaction layer was much thicker but less uniform. The compositional distribution in Figure 22d confirmed this and showed minimal change in the bulk silver compared to that in the as-brazed condition or the OX side. A zoomed-in view of the SS interface is shown in Figure 21f, where much less unoxidized reaction layers can be observed. Compared to the OX side in Figure 21c, the Ag* phase and the chromium oxides on the RE side appeared to be interlaced and no longer continuous. This finding was confirmed with the EDX line scan results in Figure 22e, in which intermixing of the Ag* phase and chromia can be observed.

The microstructural features at the YSZ interface in Figure 21g as well as the corresponding EDX line scan results in Figure 22f showed no distinctive features when compared to the as-brazed condition or the OX side in the same sample.

It was surprising that oxidized reaction layer was still present at the RE side. Two hypotheses, which may act independently or together, were proposed to explain this surprising behavior. First, as shown in Figure 12, the initial formation of the oxidized reaction layer tended to be micro-porous. Thus, there should have been a faster O_2 migration path along with the

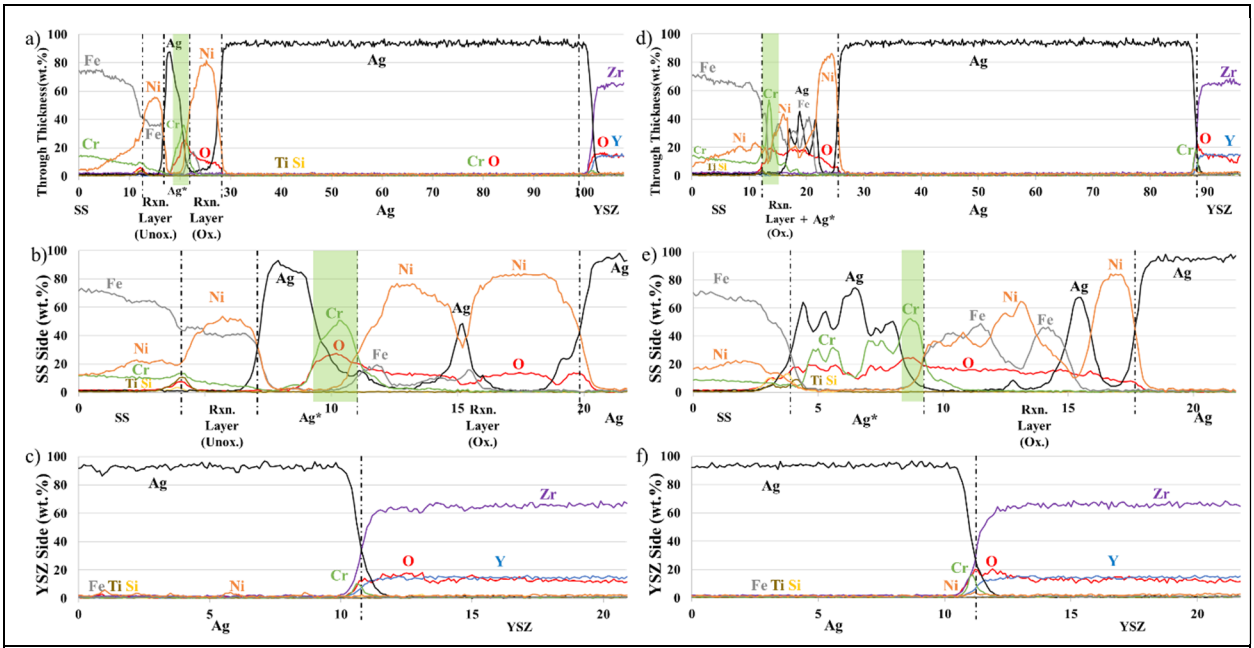

Figure 22. *Representative EDX line scan results from the 300 hour DAI tested Ag-Ni sample a) across the joint thickness, b) across the SS-braze interface, and c) across the YSZ-braze interface at the OX side; and from d) across the joint thickness, e) the SS interface, and f) the YSZ interface at the RE side of the joint. These corresponds to the red dotted line at the locations indicated in Figure 21b-g, respectively. Note, the x-axis is in microns.*

formation of the oxidized reaction layer from the OX side toward the RE side, leading to higher oxygen partial pressure (pO_2) than would otherwise be expected at the RE side. Second, Figure 22 suggests that a protective chromia layer may not have formed on the RE side, due to the scrambled nature of the reaction layer and the lower amount of oxygen on the RE side of the joint, which in turn allowed greater reaction layer oxidation than might otherwise occur. Similar phenomena has been observed in dual atmosphere high-temperature exposed SS interconnects, where surface oxidation results in a more porous and thicker oxide scale on the RE side of the interconnect compared to the air side [46-48]. This result occurred because H_2 diffusion through the protective oxide scales resulted in cation vacancies that promote Fe diffusion out of the SS to form oxides in both 430 SS [47] and 441 [48].

Very similar results (not shown) were also observed from 300 cycle DAATC tested Ag-Ni braze joints, showing good dual atmosphere as well as thermal cycling stability of the Ag-Ni braze.

5.5.5 Summary

A thorough comparison of DAI and DAATC tests on both the conventional Ag-3CuO RAB braze joints and the novel Ag-Ni braze joints yielded the following results:

1. The conventional Ag-3CuO RAB braze showed significant porosity at the SS interface caused by hydrogen reduction after both 300 hour DAI and 300 DAATC tests. Such extensive porosity would lead to early stage hermetical failure in SOFCs.
2. Braze joints produced with the novel Ag-Ni method developed as part of this award showed no porosity formation after the same DAI and DAATC tests.
3. The combined effect of dual atmosphere and thermal cycling led to similar or worse porosity formation in the Ag-3CuO braze joint even with much less time at high-temperature dual-atmosphere exposure, suggesting that the RAB braze joint was more susceptible to interfacial damage when a SOFC device is thermally cycled.
4. Ag-Ni braze joints out-performed the conventional Ag-3CuO braze in both DAI and DAATC tests, showing much improved robustness and life-times for SOFC applications.

Hence, even though the ultimate methods differed from those in the original proposal, this project was successful in meeting the project's objective of producing a new class of durable SOFC brazes.

5.6 Other Related Applications of the Ag-Ni Method

As shown in Figures 23 and 24, porous nickel layers were also used to produce dense, patterned thick film Ag circuits on various ceramic substrates (even after 5 hours of 850 °C oxidation these circuits are difficult to scrape off with a razor blade). These circuits were produced via the single-session screen printing and firing of nickel and silver inks (as in Figure 23), or via the

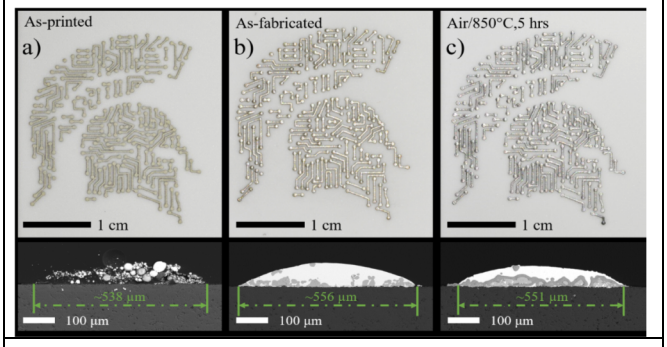

Figure 23. *Intricate Ag-Ni circuits on sapphire substrates a) after screen printing silver inks on nickel inks on sapphire substrates, b) after melting the silver via inert atmosphere heating to ~1000°C, and c) after firing the as-fabricated samples in air at 850°C for 5 hours. Note that unlike alternative methods, these circuits are dense, tolerant of green microstructural inhomogeneities, and well-bonded to the underlying substrate both after manufacturing and 5 hours at 850°C.*

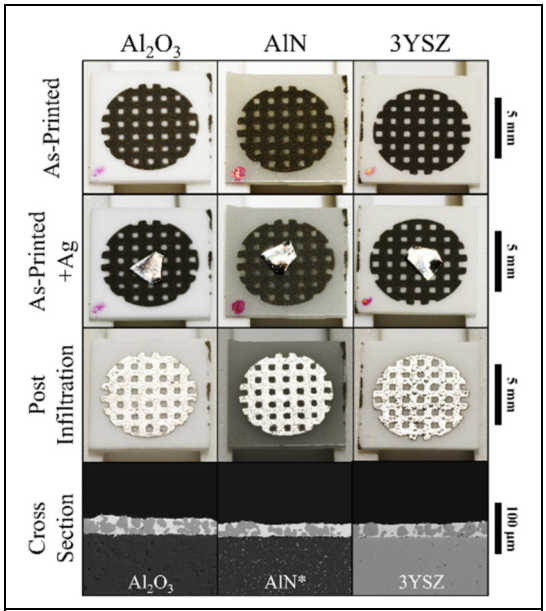

Figure 24. *Contiguous Ni-Ag circuits/current collectors on various difficult to wet ceramic substrates made by melting a silver blob atop a screen printed and partially sintered contiguous nickel pattern.*

infiltration of Ag into pre-printed, partially sintered nickel patterns (as in Figure 24). This work served as the basis for a new DOE project (DE-FE0031672) on using Ag-Ni alloys as current collectors on various SOFC materials.

6. Results Dissemination

PRODUCTS

a. Publications, Conference Papers and Presentations

i. Journal Publications:

1. Zhou, Q., T. R. Bieler and J. D. Nicholas. "Transient Porous Nickel Interlayers for Improved Silver-Based Solid Oxide Fuel Cell Brazes." *Acta Materialia* **148**: 156-162, http://dx.doi.org/10.1016/j.actamat.2018.01.061 (2018).
2. Phongpreecha, T., J. D. Nicholas, T. R. Bieler and Y. Qi. "Computational Design of Metal Oxides to Enhance the Wetting and Adhesion of Silver-based Brazes on Yttria-Stabilized-Zirconia." *Acta Materialia* **152**: 229-238, http://dx.doi.org/10.1016/j.actamat.2018.04.024 (2018).
3. Ma, Y. and J. D. Nicholas. "Mechanical, Thermal, and Electrochemical Properties of Pr Doped Ceria from Wafer Curvature Measurements." *Physical Chemistry Chemical Physics* **20**: 27350-27360, http://dx.doi.org/10.1039/c8cp04802a (2018).
4. Zhou, Q., T. R. Bieler, R. Kerr and J. D. Nicholas. "Isothermal and Rapid Thermal Cycling Tests on Ag-CuO and Ag-Ni Stainless Steel to Ytrria Stabilized Zirconia Solid Oxide Fuel Cell Brazes." *Acta Materialia* **In Preparation** (2019).
5. Zhou, Q., T. R. Bieler and J. D. Nicholas. "Controlled Wetting and Spreading of Silver on Various Ceramic Substrates." *Scripta Materialia* **In Preparation** (2019).
6. Yuxi Ma and Jason D, Nicholas, "Si-Contamination Effects on the Oxygen Surface Exchange Coefficient of Praseodymium-Doped Ceria", *Journal of Electrochemical Society*, **In Preparation** (2019)
7. Yuxi Ma and Jason D. Nicholas, "Thermo-Mechanical Properties of Praseodymium Doped Ceria Measured by High Temperature X-Ray Diffraction and Multi-beam Stress Sensor", *Physical Chemistry Chemical Physics*, **In Preparation** (2019)

ii. Books or other non-periodical, one-time publications:

Nothing to report

iii. Other Publications, conference papers and presentations:

Nothing to report

Conference Papers:

1. Zhou, Q, Bieler, TR, Nicholas, JD., "Reactive-Element-Free, Silver-Based Brazes for SOFC Applications", *SOFC XV, ECS Transactions*, pp. 1753-1767 The Electrochemical Society, Hollywood, FL, (2017).
2. Yuxi Ma and Jason D. Nicholas. "In Situ Stress, Elastic Constant, Oxygen Surface Exchange Coefficient, and Thermo-Chemical Expansion Coefficient Measurements on Praseodymium Doped Ceria Thin Films." *SOFC XV, ECS Transactions* pp. 395-403 The Electrochemical Society, Hollywood, FL, (2017).

Invited Oral Presentations:

1. Ma, Y, Nicholas, JD. A Comparison of the Wafer Curvature and X-Ray Diffractometry Determined Mechanical Properties, Defect Chemistry, and Electrochemical Performance of Praseodymium Doped Ceria Thin Films. *MS&T 2018* Columbus, OH, (October 16, 2018).
2. Zhou, Q, Bieler, TR, Kerr, R, Nicholas, JD. Reactive-Element Free, Silver-Based Brazes for SOFC Applications. *SOFC-XV* Hollywood, FL, (July 25, 2017).
3. Ma, Y, Yang, Q, Nicholas, JD. Use of a Non-Contact, In situ, and Electrode-Free Wafer Curvature Technique to "Simultaneously" Measure the Stresses, Oxygen Surface Exchange Coefficients, Elastic Constants, and Thermo-Chemical Expansion Coefficients of MIEC Thin Films. *Solid State Ionics 21* Padua, Italy, (June 20, 2017).
4. Nicholas, JD. Use of the Curvature Relaxation Technique to Simultaneously Measure the Oxygen Surface Exchange Coefficient and Stress State of Porous or Dense Films. *Materials Science & Technology 2015* Columbus, OH, (October 8, 2015).

Contributed Oral Presentations:

1. Ma, Y, Zhou, Q, Nicholas, JD. Low Temperature Silver-Based Brazing of Stainless Steel to Gadolinium Doped Ceria for SOFC Applications. *MS&T 2018* Columbus, OH, (October 18, 2018).
2. Zhou, Q, Ma, Y, Bieler, TR, Nicholas, JD. Porous Nickel Interlayer Enabled Silver Brazes and Circuits on Metals and Ceramics. *MS&T 2018* Columbus, OH, (October 15, 2018).
3. Phongpreecha, T, Nicholas, JD, Bieler, TR, Qi, Y. Computational Design of Metal Oxides to Enhance the Wetting and Adhesion of Silver-based Brazes on Yttria-Stabilized-Zirconia. *MS&T 2018* Columbus, OH, (October 18, 2018).
4. Zhou, Q, Kerr, R, Bieler, T, Nicholas, JD. Durable, Impermeable Brazes for Solid Oxide Fuel Cells. *19th Annual Department of Energy Solid Oxide Fuel Cell Workshop* Washington, DC, (June 15, 2018).
5. Ma, Y, Nicholas, JD. Using Mechano-Electro-Chemical Coupling to Measure the Thin Film Elastic Constants, Thermo-Chemical Expansion Coefficients, and Oxygen Surface Exchange Coefficients of Praseodymium Doped Ceria. *233rd Meeting of the Electrochemical Society* The Electrochemical Society, Seattle, WA, (May 14, 2018).
6. Zhou, Q, Bieler, TR, Kerr, R, Nicholas, JD. Ceramic-Metal Joining with Transient Porous Nickel Interlayer Enabled Silver Brazing. *Materials Science & Technology 2017* Pittsburgh, PA, (October 12, 2017).
7. Zhou, Q, Ma, Y, Bieler, TR, Nicholas, JD. Reactive-Element Free, Silver-Based Brazes for SOFC Applications. *SOFC-XV* Holywood, Florida, (July 24, 2017).
8. Nicholas, J, Qi, Y, Bieler, T, Zhou, Q, Ma, Y, Das, T, Phongpreecha, J. Durable, Impermeable Brazes for Solid Oxide Fuel Cells: Year 3 Review. *18th Annual Department of Energy Solid Oxide Fuel Cell Workshop* Coraopolis, PA, (June 13, 2017).
9. Nicholas, JD. Practical Considerations for Determining Thermo-Chemically Induced Stresses, Oxygen Surface Exchange Coefficients, Elastic Constants, and Thermal Expansion Coefficients from Wafer Curvature Measurements. *Pacific Rim Meeting on Electrochemical and Solid-State Science 2016* Honolulu, HI, (October 5, 2016).
10. Nicholas, J, Qi, Y, Bieler, T, Zhou, Q, Ma, Y, Das, T. Durable, Impermeable Brazes for Solid Oxide Fuel Cells: Year 2 Review. *17th Annual Department of Energy Solid Oxide Fuel Cell Workshop* Coraopolis, PA, (July 20, 2016).

11. Zhou, Q, Das, T, Ma, Y, Nicholas, JD, Qi, Y, Bieler, TR. New Braze Materials for Planar Solid Oxide Fuel Cell (SOFC) Applications. *Materials Science & Technology 2015* Columbus, Ohio, (October 6, 2015).
12. Das, T, Zhou, Q, Ma, Y, Nicholas, JD, Bieler, TR, Qi, Y. A Thermodynamics and First-Principles Based Approach to Develop Silver-Free Solid Oxide Fuel Cell Braze Alloys. *Materials Science & Technology 2015* Columbus, OH, (October 6, 2015).
13. Qi, Y, Bieler, TR, Das, T, Zhou, Q, Ma, Y, Nicholas, JD. Durable, Impermeable Brazes for Solid Oxide Fuel Cells: Year 1 Review. *16th Annual Department of Energy Solid Oxide Fuel Cell Workshop* Pittsburgh, PA, (July 15, 2015).

Poster Presentations:

1. Ma, Y, Nicholas, JD. Using a Curvature Measurement Platform to Determine In-Situ Oxygen Surface Exchange Coefficients, Thermo-Chemical Expansion Coefficients and Elastic Constants of Oxide Thin Films. *SOFC-XV* Hollywood, FL, (2017).
2. Zhou, Q, Bieler, TR, Kerr, R, Nicholas, JD. Reactive-Element-Free, Silver-Based Brazes for SOFC Applications. *SOFC-XV* Hollywood, FL, (2017).
3. Ma, Y, Nicholas, JD. Development and Application of a Wafer Curvature Platform for *In-situ* Measurements of the Physical Properties of Thin Film Materials. *18th Annual Department of Energy Solid Oxide Fuel Cell Workshop* Coreapolis, PA, (2017).
4. Zhou, Q, Bieler, TR, Kerr, R, Nicholas, JD. Reactive-Element-Free, Silver-Based Brazes for SOFC Applications. *18th Annual Department of Energy Solid Oxide Fuel Cell Workshop* Coreapolis, PA, (2017).
5. Phongpreecha, T, Nicholas, JD, Qi, Y. Theoretical Study of Ag-CuO/YSZ Braze: Adhesion Energy, Role of Oxygen, and Other Potential Oxides. *18th Annual Department of Energy Solid Oxide Fuel Cell Workshop* Coreapolis, PA, (2017).
6. Ma, Y, Zhou, Q, Das, T, Qi, Y, Bieler, TR, Nicholas, JD. Computational Predictions and Experimental Characterization of Cobalt and Copper Based Solid Oxide Fuel Cell Brazes. *17th Annual Department of Energy Solid Oxide Fuel Cell Workshop* Coraopolis, PA, (2016).
7. Zhou, Q, Ma, Y, Das, T, Qi, Y, Nicholas, JD, Bieler, TR. Nickel Based Brazes for Planar Solid Oxide Fuel Cell Applications. *17th Annual Department of Energy Solid Oxide Fuel Cell Workshop* Coraopolis, PA, (2016).
8. Qi, Y, Bieler, T, Surface, S, Kerr, R, Nicholas, JD. Durable, Impermeable Brazes for Solid Oxide Fuel Cells. *15th Annual Solid State Energy Conversion Alliance Workshop* Pittsburgh, PA, (2014).

b. Websites or other Internet Sites:

Nothing to report

c. Technologies or techniques

The Ag-Ni wetting process is invented for SOFC brazing, high temperature/power circuitry, and SOFC current collectors etc.

d. Inventions, patent applications, and/or licenses

Patent Applications:

1. J.D. Nicholas, Q. Zhou, T.R. Bieler, R.D. Kerr (2017). Brazing Methods Using Porous Interlayers and Related Articles. U.S.P.T.O. USA.
2. J.D. Nicholas, Q. Zhou, T.R. Bieler (2018). Controlled Wetting and Spreading of Metals on Substrates Using Porous Interlayers and Related Articles. U.S.P.T.O. U.S.A.

e. Other products

Nothing new to report

7. Changes/Problems

a. Changes in approach and reasons for change

i. Delphi Automotive has decided to shut down their SOFC activities. This prevented us from performing the proposed braze tests in actual SOFC devices. However basic R&D activities, including button cell tests, were conducted at both Delphi and Michigan State.

ii. Due to the inability to identify silver-free brazes with the needed set of characteristics, we instead focused our efforts on replacing the CuO wetting enhancement in conventional RAB brazes with porous nickel layers.

b. Actual or anticipated problems or delays and actions or plans to resolve them

None to report

c. Changes that have a significant impact on expenditures

Delphi donated a variety of equipment to Michigan State to fulfill this award's cost share requirements. This transaction was approved by DOE in 2017.

d. Significant changes in use of care of human subjects, vertebrate animals and/or Biohazards

None to report

e. Change in primary performance site location from that originally proposed

None to report

8. Special Reporting Requirements

None to report

9. Budgetary Information

This information will be provided under separate cover by the Michigan State Office of Contracts and Grants.

10. References

[1] Jiang SP, Chen X. Chromium Deposition and Poisoning of Cathodes of Solid Oxide Fuel Cells – A Review. International Journal of Hydrogen Energy 2014;39:505.

[2] Shi JL, Yen TS, Schubert H. Effect of Small Amounts of Additives on the Sintering of High-Purity Y-TZP. Journal of Materials Science 1997;32:1341.

[3] Ruiz-Morales JC, Canales-Vazquez J, Marrero-Lopez D, Pena-Martinez J, Tarancon A, Irvine JTS, Nunez P. Is YSZ Stable in the Presence of Cu? Journal of Materials Chemistry 2008;18:5072.

[4] Choi ID, Matlock DK, Olson DL. An Analysis of Diffusion-Induced Porosity in Cu-Ni Laminate Composites. Materials Science and Engineering a-Structural Materials Properties Microstructure and Processing 1990;124:L15.

[5] Zhao L, Perry NH, Daio T, Sasaki K, Bishop SR. Improving the Si Impurity Tolerance of $Pr_{0.1}Ce_{0.9}O_{2-\delta}$ SOFC Electrodes with Reactive Surface Additives. Chemistry of Materials 2015;27:3065.
[6] Chen D, Bishop SR, Tuller HL. Praseodymium-Cerium Oxide Thin Film Cathodes: Study of Oxygen Reduction Reaction Kinetics. Journal of Electroceramics 2012;28:62.
[7] Simons P, Ji HI, Davenport TC, Haile SM. A Piezomicrobalance System for High-temperature Mass Relaxation Characterization of Metal Oxides: A Case Study of Pr-doped Ceria. Journal of the American Ceramic Society 2017;100:1161.
[8] Nagesh VK, Pask JA. WETTING OF NICKEL BY SILVER. Journal of Materials Science 1983;18:2665.
[9] Hula RC, Edtmaier C, Holzweber M, Hutter H, Eisenmenger-Sittner C. The Wetting Behaviour of Silver on Carbon, Pure and Carburized Nickel, Cobalt and Molybdenum Substrates. Applied Surface Science 2010;256:4697.
[10] Kim JY, Hardy JS, Weil KS. Effects of CuO Content on the Wetting Behavior and Mechanical Properties of a Ag-CuO Braze for Ceramic Joining. Journal of the American Ceramic Society 2005;88:2521.
[11] Kim JY, Hardy JS, Weil KS. Silver-Copper Oxide Based Reactive Air Braze for Joining Yttria-Stabilized Zirconia. Journal of Materials Research 2005;20:636.
[12] Trumble KP. Spontaneous Infiltration of Non-Cylindrical Porosity: Close-Packed Spheres. Acta Materialia 1998;46:2363.
[13] Baker H, Okamoto H. ASM Handbook, Volume 03 - Alloy Phase Diagrams. ASM International.
[14] Hashimoto S, Fukuda Y, Kuhn M, Sato K, Yashiro K, Mizusaki J. Oxygen Nonstoichiometry and Thermo-Chemical Stability of La0.6Sr0.4Co1-yFeyO3-delta (y=0.2, 0.4, 0.6, 0.8). Solid State Ionics 2010;181:1713.
[15] Mizusaki J, Tagawa H, Naraya K, Sasamoto T. Nonstoichiometry and Thermochemical Stability of the Perovskite Type $La_{1-x}Sr_xMnO_{3-d}$. Solid State Ionics 1991;49:111.
[16] Barin I, Platzki G. Thermochemical Data of Pure Substances. Weinheim ; New York: VCH, 1995.
[17] Venkatraman M, Neumann JP. The Ag-Cr (Silver-Chromium) System. Bulletin of Alloy Phase Diagrams 1990;11:263.
[18] Weil KS, Coyle CA, Darsell JT, Xia GG, Hardy JS. Effects of Thermal Cycling and Thermal Aging on the Hermeticity and Strength of Silver-Copper Oxide Air-Brazed Seals. Journal of Power Sources 2005;152:97.
[19] Bause T, Malzbender J, Pausch M, Beck T, Singheiser L. Damage and Failure of Silver Based Ceramic/Metal Joints for SOFC Stacks. Fuel Cells 2013;13:578.
[20] Singh M, Shpargel TP, Asthana R. Brazing of yttria-stabilized zirconia (YSZ) to stainless steel using Cu, Ag, and Ti-based brazes. Journal of Materials Science 2008;43:23.
[21] Mougin J, Galerie A, Dupeux M, Rosman N, Lucazeau G, Huntz AM, Antoni L. In-situ Determination of Growth and Thermal Stresses in Chromia Scales Formed on a Ferritic Stainless Steel. Materials and Corrosion-Werkstoffe Und Korrosion 2002;53:486.
[22] Dubiel M, Chasse A, Haug J, Schneider R, Kruth H. Thermal Expansion Behaviour of Silver Examined by Extended X-Ray Absorption Fine Structure Spectroscopy. In: Hedman B, Painetta P, editors. X-Ray Absorption Fine Structure-XAFS13, vol. 882. Melville: Amer Inst Physics, 2007. p.407.

[23] Si X, Cao J, Song X, Qu Y, Feng J. Reactive Air Brazing of YSZ Ceramic with Novel Al2O3 Nanoparticles Reinforced Ag-CuO-Al2O3 Composite Filler: Microstructure and Joint Properties. Materials & Design 2017;114:176.
[24] Kubaschewski O, Hopkins BE. Oxidation of Metals and Alloys. London,: Butterworths, 1962.
[25] Niu HY, Chen XQ, Liu PT, Xing WW, Cheng XY, Li DZ, Li YY. Extra-Electron Induced Covalent Strengthening and Generalization of Intrinsic Ductile-to-Brittle Criterion. Sci Rep-Uk 2012;2:6.
[26] Lang E, Commission of the European Communities-Directorate-General for Science Research and Development. The Role of Active Elements in the Oxidation Behaviour of High Temperature Metals and Alloys. London ; New York: Elsevier Applied Science, 1989.
[27] Green SW, Stott FH. Aluminizing of Iron-Nickel-Base Alloys for Resistance to High-Temperature Gaseous Environmen. Corrosion Science 1992;33:345.
[28] Kuhn B, Wetzel FJ, Malzbender J, Steinbrech RW, Singheiser L. Mechanical Performance of Reactive-Air-Brazed (RAB) Ceramic/Metal Joints for Solid Oxide Fuel Cells at Ambient Temperature. Journal of Power Sources 2009;193:199.
[29] Phongpreecha T, Nicholas JD, Qi Y. Computational Design of Metal Oxides to Enhance the Wetting and Adhesion of Silver-based Brazes on Yttria-Stabilized-Zirconia. Acta Materialia 2018;152:229.
[30] Kuhn B, Skiera E, Brandenberg J, Li C, Beck T, Singheiser L. Mechanical Properties of Reactive Air Brazed (RAB) Metal/Ceramic Joints. Part 1: Visco-Plastic Deformation of Silver-Based Reactive Air Brazes. Advanced Engineering Materials 2014;16:1462.
[31] Kuhn B, Wessel E, Malzbender J, Steinbrech RW, Singheiser L. Effect of Isothermal Aging on the Mechanical Performance of Brazed Ceramic/Metal Joints for Planar SOFC-Stacks. International Journal of Hydrogen Energy 2010;35:9158.
[32] Poenicke A, Arnold S, Schilm J, Kusnezoff M, Michaelis A. Mechanical Properties of Reactive Air Brazed Ceramic-Metal Joints for SOFC. In: Gourley R, Walker C, editors. 5th International Brazing and Soldering Conference. Las Vegas, Nevada, USA, 2012. p.450.
[33] Bobzin K, Kopp N, Wiesner S. Influence of Filler and Base Material on the Pore Development during Reactive Air Brazing. Advanced Engineering Materials 2014;16:1456.
[34] Kim JY, Choi J-P, Weil KS. Mechanical Properties and Dual Atmosphere Tolerance of Ag-Al Based Braze. International Journal of Hydrogen Energy 2008;33:3952.
[35] Kim JY, Hardy JS, Weil S. Dual-Atmosphere Tolerance of Ag-CuO-Based Air Braze. International Journal of Hydrogen Energy 2007;32:3655.
[36] Zhou Q, Bieler TR, Nicholas JD. Transient Porous Nickel Interlayers for Improved Silver-based Solid Oxide Fuel Cell Brazes. Acta Materialia 2018;148:7.
[37] Chatzimichail R, Triantafyllou G, Tietz F, Nikolopoulos P. Interfacial properties of (Ag plus CuO) brazes used as sealing materials in SOFC stacks. Journal of Materials Science 2014;49:300.
[38] Choi JIJ, Mayr-Schmolzer W, Valenti I, Luches P, Mittendorfer F, Redinger J, Diebold U, Schmid M. Metal Adatoms and Clusters on Ultrathin Zirconia Films. Journal of Physical Chemistry C 2016;120:9920.
[39] Fergus JW. Sealants for Solid Oxide Fuel Cells. Journal of Power Sources 2005;147:46.
[40] Malzbender J, Fischer W, Steinbrech RW. Studies of Residual Stresses in Planar Solid Oxide Fuel Cells. Journal of Power Sources 2008;182:594.

[41] Ponicke A, Schilm J, Kusnezoff M, Michaelis A. Aging Behavior of Reactive Air Brazed Seals for SOFC. Fuel Cells 2015;15:735.
[42] Pavlina EJ, Meier AM, Monteleone P, Weigner JD. Development of Silver-Metal Oxide Reactive Air Braze Alloys for Electroding PZT Ceramics. Journal of Materials Science 2007;42:705.
[43] Chen H, Li LJ, Kemps R, Michielsen B, Jacobs M, Snijkers F, Middelkoop V. Reactive Air Brazing for Sealing Mixed Ionic Electronic Conducting Hollow Fibre Membranes. Acta Materialia 2015;88:74.
[44] Weil KS, Kim JY, Hardy JS. Reactive air brazing: A novel method of sealing SOFCs and other solid-state electrochemical devices. Electrochemical and Solid State Letters 2005;8:A133.
[45] Chatzimichail R, Triantafyllou G, Tietz F, Nikolopoulos P. Interfacial Properties of (Ag+CuO) Brazes Used as Sealing Materials in SOFC Stacks. Journal of Materials Science 2014;49:300.
[46] Leonard ME, Amendola R, Gannon PE, Shong WJ, Liu CK. High-Temperature (800 Degrees C) Dual Atmosphere Corrosion of Electroless Nickel-Plated Ferritic Stainless Steel. International Journal of Hydrogen Energy 2014;39:15746.
[47] Li J, Yan D, Gong YP, Jiang YX, Li J, Pu J, Chi B, Jian L. Investigation of Anomalous Oxidation Behavior of SUS430 Alloy in Solid Oxide Fuel Cell Dual Atmosphere. Journal of the Electrochemical Society 2017;164:C945.
[48] Alnegren P, Sattari M, Svensson JE, Froitzheim J. Severe Dual Atmosphere Effect at 600 Degrees C for Stainless Steel 441. Journal of Power Sources 2016;301:170.